Chemical Engineering Journal 477 (2023) 147155

Contents lists available at ScienceDirect

Chemical Engineering Journal

journal homepage: www.elsevier.com/locate/cej

Remarkably boosted water oxidation activity and dynamic stability at large-current–density of $Ni(OH)_2$ nanosheet arrays by Fe ion association and underlying mechanism

Zanling Huang [a], Abebe Reda Woldu [a], Xiang Peng [c], Paul K. Chu [d], Qing-Xiao Tong [a,*], Liangsheng Hu [a,b,*]

[a] Department of Chemistry and Key Laboratory for Preparation and Application of Ordered Structural Materials of Guangdong Province, Shantou University, Shantou, 515063, PR China
[b] Chemistry and Chemical Engineering Guangdong Laboratory, Shantou, 515063, PR China
[c] Hubei Key Laboratory of Plasma Chemistry and Advanced Materials, School of Materials Science and Engineering, Wuhan Institute of Technology, Wuhan, 430205, PR China
[d] Department of Physics, Department of Materials Science and Engineering, and Department of Biomedical Engineering, City University of Hong Kong, Tat Chee Avenue, Kowloon, Hong Kong, China

ARTICLE INFO

Keywords:
Oxygen evolution reaction
$Ni(OH)_2$
Fe(III)-catalysis
Dynamic stability
Water splitting

ABSTRACT

There have been reports about the promoted oxygen evolution reaction (OER) activity by adding of Fe ions into alkaline electrolytes for Ni-based catalysts. However, the origin and reason for the OER activity improvement remains vague. In this work, we endeavor to recognize the activity enhancement by a series of control and *in/ex situ* experiments. After introducing of 500 μM of Fe(III) to 1.0 M KOH, the current density of $Ni(OH)_2$ nanosheet arrays at 1.6 V increases substantially from 36 to 1052 mA cm^{-2}, and the overpotentials required to reach 100 mA cm^{-2} reduces obviously from 422 to 269 mV and 1,000 mA cm^{-2} from 616 to 367 mV. The electrochemical water splitting electrolyzer with $Ni(OH)_2$ as anode and Pt/Ni-Mo as cathode exhibits robust activity and stability for 1,000 h at 1,000 mA cm^{-2} @ 1.7 V. *In/ex situ* electrochemical analysis, morphology and structure characterizations reveal that Fe(III) serves as the active sites and promotes the OER kinetics by two ways: (1) mainly cyclical formation of intermediates (Fe(III) → (Ni)Fe^{x+} → (Ni)Fe-OH → (Ni)Fe-O → (Ni)Fe-OOH → Fe(III) (+O_2)) on the electrode/electrolyte interface and (2) growth of the Ni-FeOOH/Fe-NiOOH interface on the surface of Ni $(OH)_2$. The results provide insights into the Fe(III)-catalysis effect and guidance for the development of high-performance commercial water-splitting systems.

1. Introduction

The growing concern about energy depletion and environmental problems make it urgent to develop green and sustainable energy sources as alternatives to fossil fuels [1]. Hydrogen, as a clean and renewable energy carrier with high gravimetric energy, is regarded as one of the most promising energy sources to replace conventional fossil fuels [2]. Accordingly, water electrolysis, involving the hydrogen evolution reaction (HER) on the cathode and the oxygen evolution reaction (OER) on the anode, has attracted great attention as a clean and promising technology to produce H_2, where the sluggish kinetics of the OER seriously restricts the efficiency of the overall water splitting [3–6]. Therefore, efficient OER electrocatalysts are urgently demanded to reduce the actual required potential for OER and improve the total hydrogen generation efficiency. Although noble metal-based oxides such as RuO_2 and IrO_2, have shown high OER catalytic activity in acidic media, the large-scale commercial implementation is hindered by the high cost and limited natural reserves [7]. In this regard, tremendous efforts have been devoted to alkaline OER using earth-abundant non-precious transition metals like Ni, Co, and Fe with high activity and stability [8]. Among the various active OER catalysts, mixed NiFe-based materials (e.g., oxyhydroxides, alloy, oxides, *etc*.) have stood out as one of the most promising candidates due to the earth abundance and superior OER efficiency in alkaline electrolytes [9–13].

Numerous efforts including heterostructure construction [14,15], interfacial interaction [16], vacancy-modifying [17,18], and

* Corresponding authors.
E-mail addresses: qxtong@stu.edu.cn (Q.-X. Tong), lshu@stu.edu.cn (L. Hu).

https://doi.org/10.1016/j.cej.2023.147155
Received 15 August 2023; Received in revised form 7 October 2023; Accepted 3 November 2023
Available online 4 November 2023

heteroatom-doping [19] have been developed to optimize the OER performance of mixed NiFe-based materials, achieving excellent activity for OER. Besides the activity, another concern about mixed NiFe-based materials is their stability, which is also important for commercial water splitting system. In particular, the strict industrial criteria of water electrolyzer requires an exceptional electrocatalyst to operate with robust stability at high current density above 500 mA cm^{-2} with overpotential below 300 mV [20–23]. Recent studies have shown that the OER deactivation is a common issue among the mixed NiFe-based electrocatalysts under prolonged OER conditions, but the causes and strategies to solve the bottleneck are still being investigated [24–26]. In general, NiFe-based materials will experience severe metal dissolution at high OER potential and phase segregation due to selective redeposition of dissolved Ni and Fe cations, resulting in activity decay, not to mention at even higher current densities for commercial application. Much effort have been made to enhance the stability and lifetime of mixed Ni-Fe-based materials for commercial application. For instance, Chen et al. have studied the deactivation mechanism of NiFe-LDH in OER and the acidic environment in the interlayers of bulk NiFe-LDH is responsible for metal dissolution in the alkaline electrolyte. Exfoliating multilayered NiFe-LDH into atomically thin nanosheets can improve the OER stability with time under industrial conditions (e.g., at 80 °C and 500 mA cm^{-2}). However, OER degradation is still unavoidable because of phase segregation of FeOOH and NiOOH in the basal planes of the NiFe-LDH nanosheets [27]. Construction of atomic cation-vacancies on the basal plane of NiFe-LDH is an effective way to suppress metal dissolution under OER conditions and improve the stability. However, the current density is about 100 mA cm^{-2}, which cannot still satisfy the requirement for commercial applications [28]. Kuai and co-workers have developed an *in situ* electrochemical reduction strategy to refresh the catalytic activity of electrocatalysts degraded by FeOOH segregation and enhance the catalyst stability [29]. However, the intermittent reduction technique is unsuitable for industrial applications, as the application of an instantaneous reverse current for catalyst regeneration causes irreversible damage to the counter electrode [30]. This has spurred the search for alternative, simple, and practical strategies to endow mixed NiFe-based materials with both the desirable activity and durability for commercial applications.

Besides designing and synthesizing electrocatalysts, recent findings have shown that the extrinsic cations in alkaline electrolyte exerted significant influence on the OER activity of Ni-based electrocatalysts and furnished a novel approach to improve the OER efficiency. With regard to Ni-based OER electrocatalysts, extrinsic cations in the alkaline medium affect the OER characteristics. Fe impurities were found to enhance the OER activity of Ni-oxide already in 1987 [31]. Subsequently, huge efforts have been focused on understanding the role of Fe and the synthesis of highly active anodes to maximize the activity [32,33], but the exact role of "Fe^{3+} effects" [33] is still not fully understood. Moreover, it has been reported that there exists dynamic metal ion exchange at the interface between the catalyst surface and the electrolyte during the OER process due to the dissolution/re-deposition of metallic species [29,34–36]. Inspired by this, we consider the addition of sufficient Fe cations as a feasible strategy to boost the OER activity and stability by dynamically adjusting the amounts of metal cations in

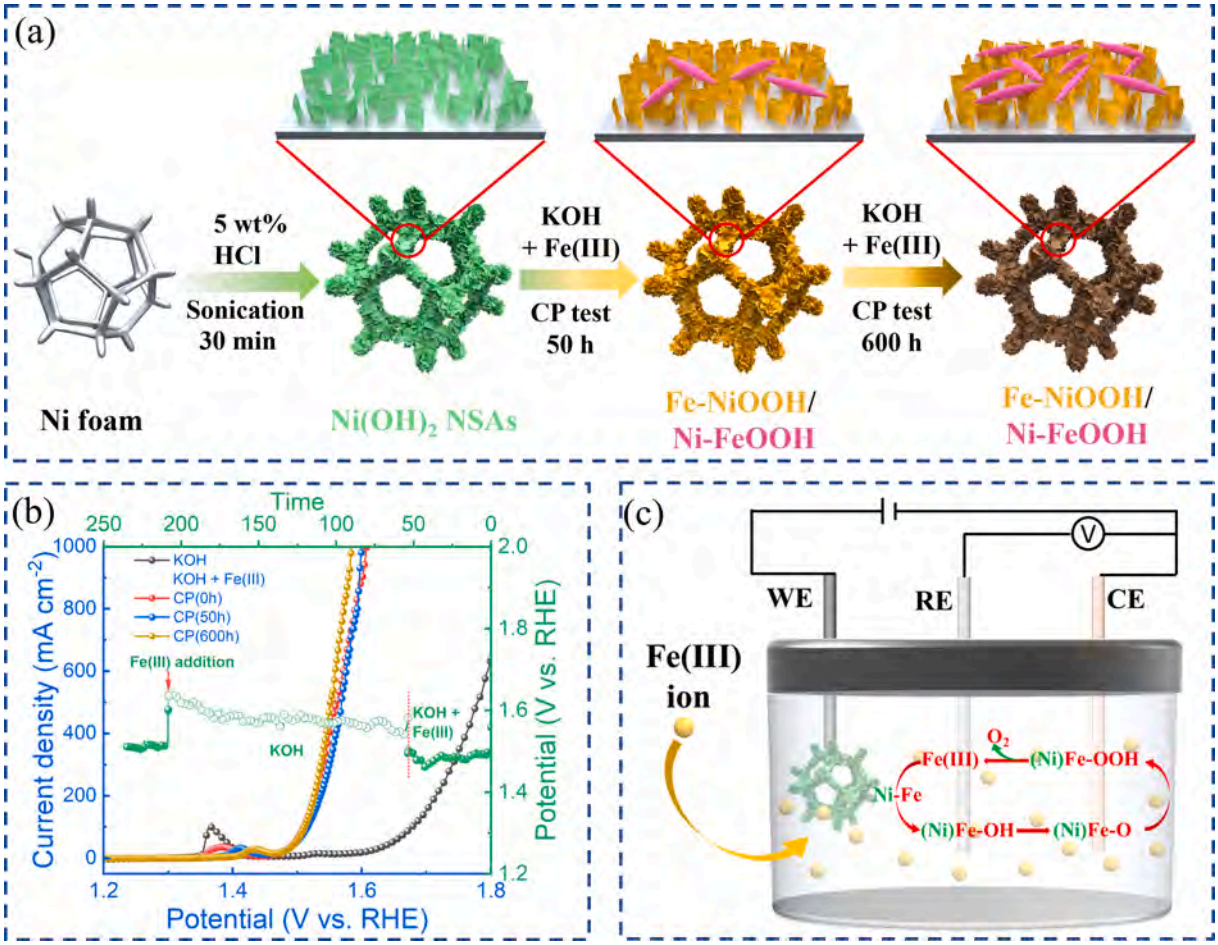

Scheme 1. Demonstration of Fe(III)-catalyzed OER on the $Ni(OH)_2$. (a) The preparation process of $Ni(OH)_2$ nanosheet arrays (NSAs) and the structure evolution during the chronopotentiometry (CP) test in 1.0 M KOH with 500 μM Fe(III) (KOH + Fe(III)) for different time; (b) The LSV and CP plots of $Ni(OH)_2$ in KOH and KOH + Fe(III); (c) Proposed Fe(III)-catalyzed mechanism of OER on $Ni(OH)_2$ in alkaline electrolyte. WE: working electrode, RE: reference electrode, CE: counter electrode.

the solution during the activation process, which can solve the problem of metal dissolution and phase segregation.

Herein, sufficient Fe(III) cations are introduced to the electrolyte to enhance the OER catalytic efficiency and dynamic stability. The $Ni(OH)_2$ with Fe(III)-catalysis delivers improved OER performance by adding Fe (III) cations to the electrolyte. Fe(III) serves as the active sites and promotes the OER kinetics by two ways: (1) Cyclical formation of intermediates (Fe(III) → (Ni)Fe^{x+} → (Ni)Fe-OH → (Ni)Fe-O → (Ni)Fe-OOH → Fe(III) (+O_2)) on the electrode/electrolyte interface and (2) Growth of the Fe-NiOOH/Ni-FeOOH interfaces on the surface of Ni $(OH)_2$ (Scheme 1). For the commercial application, a water splitting electrolyzer with $Ni(OH)_2$ as anode and reported Pt/Ni-Mo as cathode is demonstrated. The Fe(III)-catalyzed electrolyzer requires only 1.7 V to reach 1,000 mA cm^{-2} and remains stable for 1,000 h under different operating conditions (1.0 or 3.0 M KOH and 25 or 60 °C).

2. Experimental section

2.1. Chemicals and reagents

All the chemical and reagents in this work were used directly without pre-purification. The Ni foam was acquired from SaiBo Electrochemical Materials Network. Ferric(III) nitrate [$Fe(NO_3)_3{\cdot}9H_2O$] (99 %) and ammonium molybdate tetrahydrate [$(NH_4)_6Mo_7O_{24}{\cdot}4H_2O$] (99 %) were obtained from Saen Chemical Technology (Shanghai) Co., Ltd. Potassium hydroxide (KOH, AR), hydrochloric acid, and nickle(II) nitrate [$Ni(NO_3)_2{\cdot}6H_2O$] (AR) were purchased from Xilong Scientific Co., Ltd. Chloroplatinic acid hexahydrate [$H_2PtCl_6{\cdot}6H_2O$] (AR, Pt ≥ 37.5 %) was bought from Shanghai Macklin Biochemical Co., Ltd. All the solution and electrolytes were prepared with deionized water. For the Fe-free measurement for comparison, the KOH electrolyte was purified according to a previous report [32].

2.2. Preparation of electrodes

The $Ni(OH)_2$ nanosheet arrays (NSAs) electrode was prepared on Ni foam via a facile ultrasonic method according to a previous report [37]. The Ni foam was cut into pieces of 0.5 × 2 cm^2 and sonicated in 5 wt% HCl solution for 30 min. The $Ni(OH)_2$ NSAs were obtained after the ultrasonic-treated Ni foam being rinsing with deionized water and drying in vacuum oven (40 °C) overnight. The cathode of the water splitting electrolyzer, Pt/Ni-Mo [38], and the compared NiFe-LDH electrode [39] were prepared according to the previous reports.

2.3. Characterization

The morphology and microstructure of the materials were characterized by field-emission scanning electron microscopy (FE-SEM, Gemini 300) and scanning transmission electron microscopy (TEM, FEI Titan G2 60–300) coupled with energy dispersive spectroscopy (EDS). The crystal phases and chemical compositions were identified by X-ray powder diffraction (XRD, Mini Flex 600) and X-ray photoelectron spectroscopy (XPS, Thermo Fisher Scientific K-alpha). *In situ* Raman scattering was conducted on the HR RamLab Raman Spectrometer (excitation wavelength of 532 nm).

2.4. Electrochemical measurements

The electrochemical characterization was performed on the CHI660E workstation with a three-electrode system comprising $Ni(OH)_2$ NSAs electrode (0.5 × 0.5 cm^2) as the working electrode, calomel (SCE) electrode as the reference electrode, and Pt wire as the counter electrode. The 1.0 M KOH without and with $Fe(NO_3)_3{\cdot}9H_2O$ of proper concentrations were used as the electrolytes. 50 cyclic voltammetric cycles (CVs) within 0.1–0.6 V (vs. SCE) at scanning rate of 10 mV s^{-1} were performed beforehand to stabilize the OER current. The linear sweep voltammetry (LSV) polarization curves were obtained at 5 mV s^{-1} within 0.1–0.75 V (vs. SCE) with 100 % *i*R compensation. To determine the double-layer capacitance (C_{dl}), the CV curves were recorded at various scanning rates of 2, 4, 6, 8, and 10 mV s^{-1} in the non-Faradaic potential window of 0.1–0.2 V (vs. SCE). The *in situ* electrochemical impedance spectroscopy (EIS) was conducted with the potential and frequency ranging from 1.1 to 1.7 V and 0.1 to 100 kHz, respectively. In the stability test, the chronopotentiometry (CP) test was performed at 1000 mA cm^{-2}.

3. Results and discussions

3.1. The OER performance of $Ni(OH)_2$ boosted by Fe(III)

To meet the commercial application, the $Ni(OH)_2$ NSAs electrode was synthesized via a simple sonicated treatment of Ni foam for 30 min. FE-SEM images of Ni foam and $Ni(OH)_2$ NSAs in the same magnifications (Fig. S1**a and S1b**) display a nanostructure assembled by well-interconnected NSAs on the surface of Ni foam in the as-prepared Ni $(OH)_2$ sample, compared with the smooth surface of untreated Ni foam. The NSAs with voids are advantageous for the interaction with reactants. The double-layer capacitances (C_{dl}) measurements are conducted to estimate the electrochemical active surface area (ECSA) of Ni foam and $Ni(OH)_2$ (**Fig. S2**). The $Ni(OH)_2$ NSAs electrode possesses a C_{dl} value of 8.4 mF cm^{-2}, which is larger than that of Ni foam (4.6 mF cm^{-2}) (Fig. S2**c**), indicating more active sites and porous structure of the Ni $(OH)_2$ NSAs. Thus, the $Ni(OH)_2$ NSAs could not only bring abundant active sites but also favor the penetration of the electrolyte into the interior structure, which is advantageous for electrolysis.

To prove the enhancement effect of Fe(III) ions on the performance of $Ni(OH)_2$ NSAs electrode, the OER electrocatalytic performance is evaluated and compared by LSVs initially using three-electrode system in purified KOH (pKOH, the analytic reagent KOH usually contains trace Fe impurity), unpurified KOH (KOH) solution without and with different concentration of Fe(III). As shown in **Fig. S3**, the LSV curve in pKOH shows smaller current density than that in unpurified KOH, indicating trace Fe(III) in solution can enhance the OER activity of $Ni(OH)_2$ NSAs. Intentionally, Fe(III) ions with different concentrations were added into KOH for boosting OER performance. As shown in Fig. 1**a**, the LSV curves obtained from Fe(III) containing electrolytes demonstrate enhanced current density than that from KOH solution, even with the low Fe(III) concentration of 0.5 μM, which reveals the promoting effect of Fe(III) on the catalytic activity of $Ni(OH)_2$ electrode. The OER current density increases with the increment of Fe(III) concentration until 500 μM. Catalyzed by Fe(III) of 500 μM, the system achieves the best OER properties. Noteworthily, $Ni(OH)_2$ electrode in KOH + 500 μM Fe(III) even show much better OER activity than that of NiFe-LDH in KOH (Fig. 1**b**). The current density at 1.6 V (J@1.6 V) increases substantially from 36 to 1052 mA cm^{-2}, and the overpotentials required to reach 100 mA cm^{-2} (η_{100}) reduces obviously from 422 to 269 mV (Fig. 1**c**). Meanwhile, the onset potential of $Ni(OH)_2$ in KOH + Fe(III) is 1.45 V, which is much lower than that in KOH (1.60 V) (**Fig. S4**). The Tafel plots were derived from LSVs to compare the OER kinetics in 1.0 M KOH (denoted as KOH) and 1.0 M KOH with 500 μM Fe(III) (denoted as KOH + Fe(III)) electrolytes. The Tafel slope of the $Ni(OH)_2$ electrode in KOH + Fe(III) is 51.9 mV dec^{-1}, which is much lower than that in KOH (108.2 mV dec^{-1}), demonstrating that the adsorption of OH^- is relatively easier and strongly catalyzed by Fe(III) (Fig. 1**d**) [40]. For comparison, Ni foam was also employed as the working electrode and tested in KOH and KOH + Fe(III). Similarly, the LSV curves show obviously larger current density in KOH + Fe(III) than that in KOH (Fig. S5**a**). Moreover, the $Ni(OH)_2$ catalyzed by Fe(III) delivers higher OER activity than Ni foam (Fig. S5**b**). Noteworthy, the oxidation peak of $Ni(OH)_2$ increases from 1.36 V in KOH to 1.38 V in KOH + Fe(III), indicating that the Fe incorporation into the $Ni(OH)_2$. These results reveal Fe(III) improves the OER activity of Ni $(OH)_2$ NSAs.

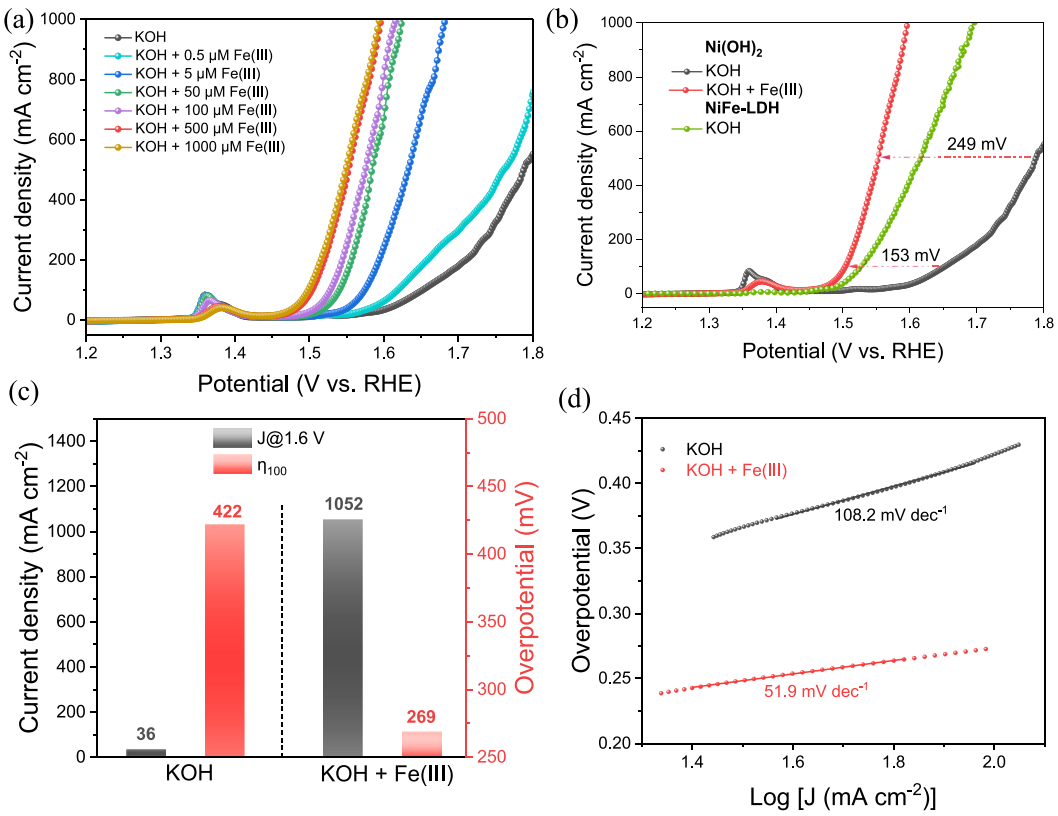

Fig. 1. (a) The LSV curves of $Ni(OH)_2$ in 1.0 M KOH with and without different concentration of Fe(III); (b) The comparisons of LSV curves of $Ni(OH)_2$ in 1.0 M KOH (KOH) and 1.0 M KOH with 500 μM Fe(III) (KOH + Fe(III)), and NiFe-LDH in KOH; (c) Comparisons of J@1.6 V and η_{100} of $Ni(OH)_2$ in KOH and KOH + Fe(III); (d) The Tafel plots of $Ni(OH)_2$ in KOH and KOH + Fe(III).

3.2. *The mechanism of Fe(III)-catalysis on $Ni(OH)_2$*

To reveal the mechanism of Fe(III) catalysis and investigate the factors underpinning the OER activity trend, *in situ* electrochemical impedance spectroscopy (EIS) analysis was conducted at various potentials. The Bode phase diagrams and Nyquist plots in KOH and KOH + Fe(III) are shown in Fig. 2**a, 2b and S6**, respectively. For the EIS spectra, the low-frequency and high-frequency regions are associated with OER and the electrooxidation inside the electrode, respectively [41]. With the increase of potential, the Bode phase diagrams in KOH and KOH + Fe (III) show the inflection points (greenish-blue circle, an area with a marked change in curvature) at 1.6 V and 1.5 V in the low-frequency region, respectively (Fig. 2**a and 2b**), which are in the same trend with the onset potentials in Fig. 1**a** [42]. In the high frequency region, the phase angle value in KOH + Fe(III) is lower than that in KOH, which means faster reaction kinetics in KOH + Fe(III) [42]. The Fe(III) addition contributes to the fast transfer of electrically active species (OH^-) and thus facilitating the OER process [40,43,44]. In the Nyquist plots (Fig. S6**c and S6d**), the R_{ct} decreases with larger applied potential. The $Ni(OH)_2$ in KOH + Fe(III) shows smaller semicircle at all potentials, indicating lower charge transfer resistance and a faster reaction rate catalyzed by Fe(III). Furthermore, the electrochemical characteristics and OER activity of $Ni(OH)_2$ electrodes in KOH and KOH + Fe(III) were first investigated by 40 cycle CVs with a scanning rate of 5 mV s^{-1}. The CV curves include information of phase transition and OER activity based on the redox features of Ni. The LSV curves exhibit a wide anodic peak at about 1.37 V due to the change of Ni^{2+} to Ni^{3+}. In KOH (Fig. 2**c**), a small oxidative peak at 1.53 V is attributed to the formation of a small amount of Ni^{4+} oxidation state [32,45]. The OER current density increases with increasing CV cycles due to more Ni^{2+} to Ni^{3+}/Ni^{4+} transition beneath the surface of $Ni(OH)_2$. However, in KOH + Fe(III) (Fig. 2**d**), the redox peak for the Ni^{2+} to Ni^{3+} transition was positively shifted compared to the peaks in KOH (1.37 V) due to the incorporation of Fe, ascribing the difficulty in oxidizing Ni^{2+} to Ni^{3+} [32], and no peaks corresponding to the oxidation peaks of Ni^{4+} were observed, which would be obscured by the robust OER current delivered at the oxidation potential. Altogether suggests that the Fe(III)-containing system lowers the overpotential consumption. The current density at 1.55 V keeps almost constant compared with that in KOH, which indicates the catalysis effect of Fe(III) plays the main role. *Operando* Raman spectra of the $Ni(OH)_2$ electrode in both KOH and KOH + Fe(III) were collected to investigate the process of surface reconstruction during the real-time catalytic process (Fig. 2**e and 2f**). It was conducted in the potential range from 0.32 to 0.62 V (vs. Ag/AgCl) with an interval of 0.05 V. A characteristic peak located at 487 cm^{-1} assigned to the characteristic mode of $Ni(OH)_2$ [46] is observed from 0.32 to 0.52 V in KOH and from 0.32 to 0.37 V in KOH + Fe(III). Two new characteristic peaks at 472 and 552 cm^{-1} emerge from 0.57 V in KOH attributed to the depolarized E_g mode (bending, denoted as B peak) and polarized A1g mode (stretching, denoted as S peak) of γ-NiOOH, respectively [47,48]. In KOH + Fe(III), the two new peaks appear from 0.42 V and slightly shift to a lower frequency of 471 and 552 cm^{-1}. The characteristic peaks of NiOOH appeared at 0.57 V and 0.42 V in KOH and KOH + Fe(III) are in the same trend with the onset potentials of 1.60 V and 1.45 V (vs. RHE) in **Fig. S4**. On both the *in situ* Raman and LSV measurements, the Fe(III) containing system exhibited a shift to a lower anodic potential by 150 mV, indicating that Fe(III) greatly improves the OER activity by facilitating the Ni^{2+} to Ni^{4+} transition, and thus, decrease the overpotential consumption for the transformation of $Ni(OH)_2$ to γ-NiOOH [46,48–51]. The high ratio of B peak to S peak (I_B/I_S) also demonstrates the formation of γ-NiOOH, which contains highly oxidized nickel species and provides higher OER activity [52,53]. The $Ni(OH)_2$ in KOH + Fe(III) shows higher I_B/I_S than that in KOH during the whole OER process, confirming the higher OER activity catalyzed by Fe(III). To investigate the change of

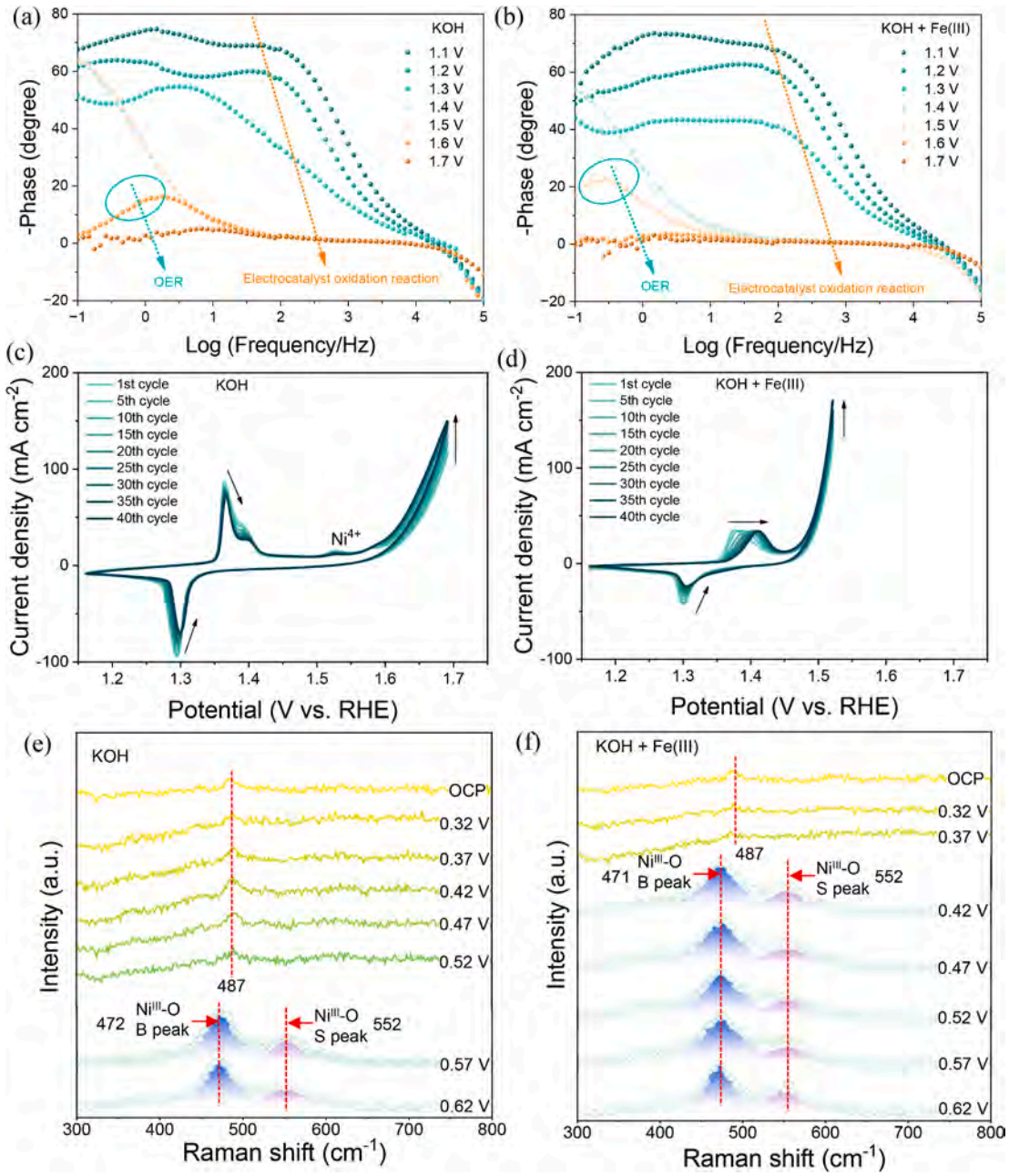

Fig. 2. Bode-phase plots of $Ni(OH)_2$ for different applied potentials in (a) KOH and (b) KOH + Fe(III); CV profiles for 40 cycles of the $Ni(OH)_2$ in (c) KOH and (d) KOH + Fe(III) at a scanning rate of 5 mV s^{-1}; *In situ* Raman spectra of $Ni(OH)_2$ measured in (e) KOH, and (f) KOH + Fe(III) in the potential range from 0.32 to 0.62 V (vs. Ag/AgCl) with an interval of 0.05 V.

ECSA after Fe(III) addition, the C_{dl} measurements were conducted on Ni $(OH)_2$ in KOH and KOH + Fe(III) (Fig. S7). Interestingly, the C_{dl} values in KOH + Fe(III) (6.8 mF cm^{-2}) decreases slightly than that in KOH (8.4 mF cm^{-2}), revealing that the OER enhancement in the system could be attributed to the catalysis effect of Fe(III). The above electrochemical and Raman data indicate that the Fe(III) improves the OER activity of Ni $(OH)_2$ and would further promote the surface phase evolution during electrochemical activation.

Previous reports declare that the active catalytic interface can be updated *in situ* by directional adjustment of dynamic equilibrium [54], but the mechanism is still elusive. Besides, the achieved current density and attended time are far from satisfying the strict criteria of commercial application. To ascertain the concrete enhancement effect of Fe(III) and the stability in the Fe(III) containing system, the LSVs and chronopotentiometry (CP) measurements at a larger current density of 1000 mA cm^{-2} for 50 h of $Ni(OH)_2$ electrode in KOH and KOH + Fe(III), and Fe(III)-activated/absorbed $Ni(OH)_2$ in KOH were compared. Fe(III)-activated $Ni(OH)_2$ was preactivated in KOH + Fe(III) by 50 CVs in the range of 0.1–0.6 V (vs. SCE), while the Fe(III) absorbed $Ni(OH)_2$ was absorbed in KOH + Fe(III) for the same time. As shown in Fig. 3**a**, the Ni $(OH)_2$ electrode in KOH + Fe(III) and the Fe(III)-activated/absorbed Ni $(OH)_2$ all demonstrate higher current density than that in KOH, indicating the Fe(III) species offer significant contribution to the OER activity. Moreover, the OER performance of Fe(III)-activated $Ni(OH)_2$ is better than that of absorbed one, which implies more active intermediate species generate on the surface of electrode through pre-activation. However, both the pristine $Ni(OH)_2$ and Fe(III)-activated/absorbed Ni $(OH)_2$ electrodes show unsatisfying OER stability (Fig. 3**b**) compared with that in KOH + Fe(III). As shown in Fig. 3**b**, both the potentials of CP curves in KOH and KOH + Fe(III) display decrement in the beginning,

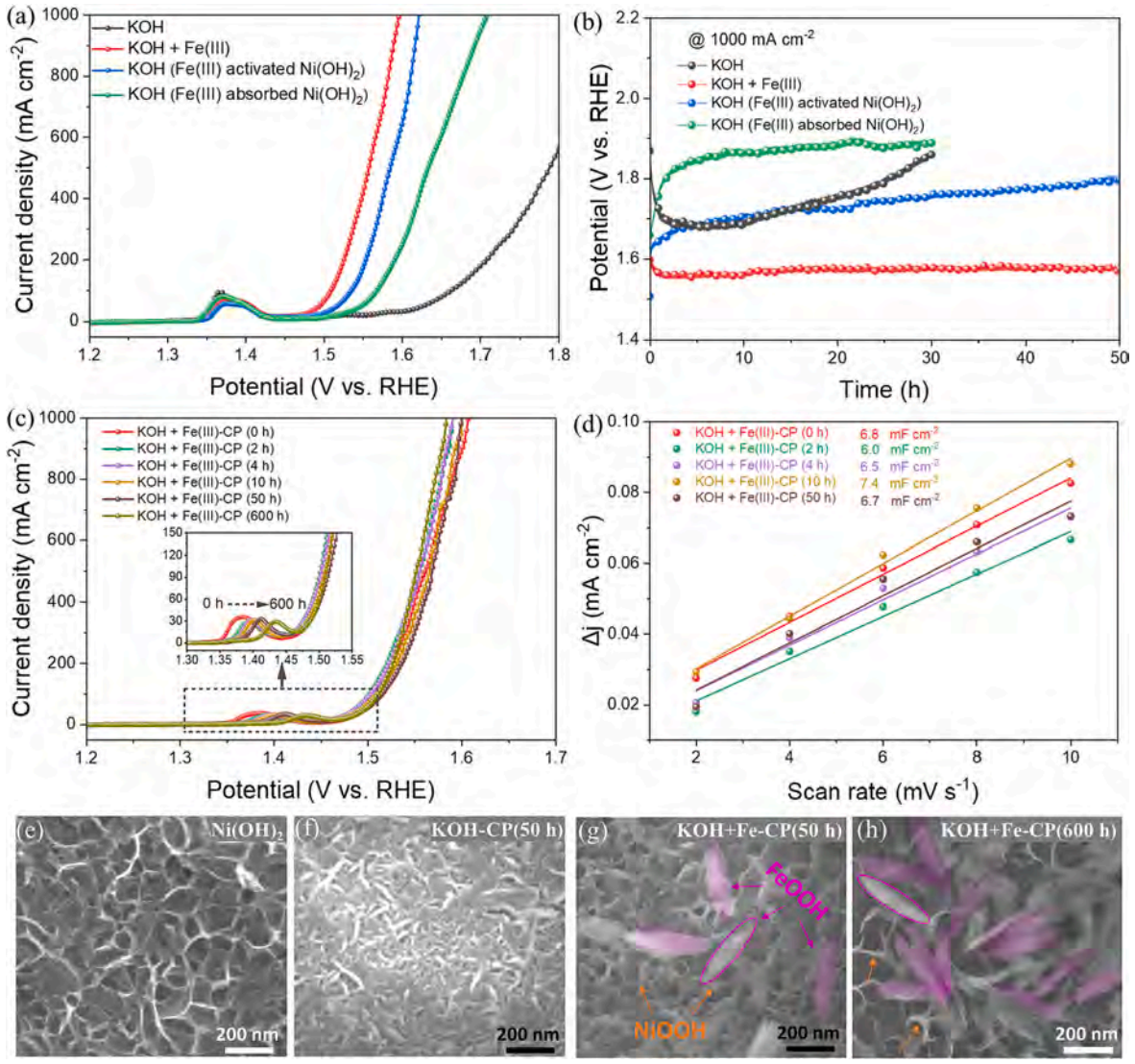

Fig. 3. (a) LSV curves and (b) CP plots of the $Ni(OH)_2$, Fe(III)-activated and Fe(III)-absorbed $Ni(OH)_2$ obtained from KOH as well as the $Ni(OH)_2$ obtained from KOH + Fe(III); (c) The LSV curves and (d) C_{dl} values of the $Ni(OH)_2$ obtained from KOH + Fe(III) after the CP test for different time (0, 2, 4, 10, 50, 600 h); SEM images of (e) $Ni(OH)_2$, $Ni(OH)_2$ after CP test for 50 h (f) in KOH, 50 h (g) and (h) 600 h in KOH + Fe(III).

which might due to the activation of the $Ni(OH)_2$ electrode. After that, the CP curve in KOH shows potential increases evidently, indicating the severe activity degradation of $Ni(OH)_2$. While in KOH + Fe(III), the potential keeps constant, revealing Fe(III) plays a key role in realizing robust stability. To further illustrate the enhancement effect of Fe(III) in this system, we compare the OER activity by LSV measurements (**Fig. S8a and 3c**) and the C_{dl} values (**Fig. S8b, S9 and 3d**) of $Ni(OH)_2$ after testing in KOH + Fe(III) for different time (0, 2, 4, 10, 50, 600 h). Surprisingly, the electrode shows no evident changes in OER current density and C_{dl} values even after 600 h compared with the initial test. The oxidation peak of the transition from Ni^{2+} to Ni^{3+} shift toward higher potential with testing time, indicative of more and more Fe(III) incorporation with testing time (the inset in Fig. 3**c**). However, the OER performances almost keep unchanged over testing time, suggesting that the promoted OER activity is not mainly ascribed to the formation of NiFe bimetallic compounds.

To obtain insight into the evolution of the surface structure and the relationship between the catalytic activity and the surface structures of the electrodes, the morphology of the pristine $Ni(OH)_2$, $Ni(OH)_2$ electrode after CP testing for 50 h in KOH and KOH + Fe(III), and 600 h in KOH + Fe(III) were characterized. The FE-SEM images in Fig. 3**e and 3f** show $Ni(OH)_2$ electrodes before and after testing in KOH. Compared to the fresh $Ni(OH)_2$ sample, the nanosheet structures collapse after running for 50 h, which might result in the OER activity deterioration (Fig. 3**b**). Interestingly, the nanosheets are intact and new nanofusiform particles with the length of ~ 200 nm and width of ~ 50 nm are deposited on the surface of the electrode after testing in KOH + Fe(III) for 50 h (Fig. 3**g**) and the number of the particles substantially increase after testing for 600 h (Fig. 3**h and S10**). The XRD patterns are used for identifying the structure of the samples (**Fig. S11**). However, only the peaks of Ni metal are observed on both the samples after testing in KOH and KOH + Fe(III), the same as pristine $Ni(OH)_2$ sample, maybe due to the low content or amorphous structure of the intermediates. The TEM image exhibits the same nanosheet array and nanospindle morphology of the sample after CP testing for 50 h in KOH + Fe(III) (Fig. 4**a**) in good agreement with the SEM images, while the HRTEM (Fig. 4**b**) shows that the nanosheet consists of NiOOH and the nanospindle of FeOOH structure. The interplanar spacing of 0.179 nm and 0.295 nm are assigned to NiOOH(1 0 8) and FeOOH(2 2 0), respectively. The selected area electron diffraction (SAED) pattern shows a set of diffraction dots (Fig. 4**c**), corresponding to the (1 1 0) plane of NiOOH, (3 2 4), (4 0 0), and (4 1 0) planes of FeOOH, respectively, which confirms that the surface species

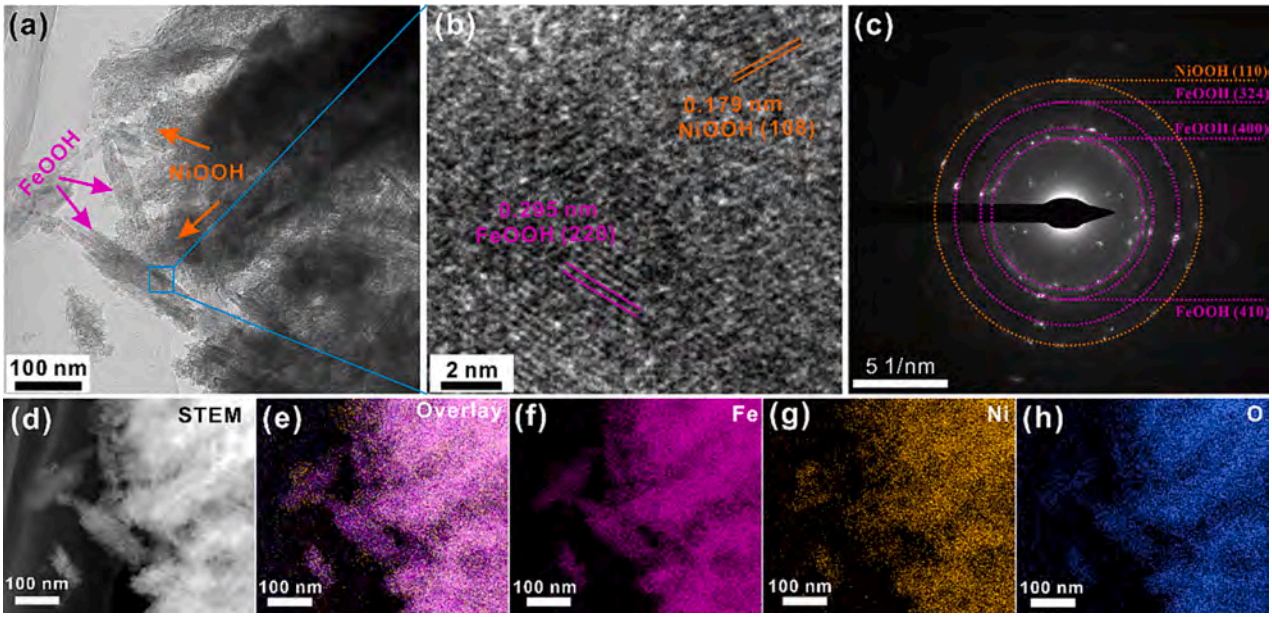

Fig. 4. (a) TEM image, (b) HRTEM image, (c) SAED pattern, (d) HAADF-STEM images and (e-h) EDS maps of the $Ni(OH)_2$ after CP test for 50 h in KOH + Fe(III).

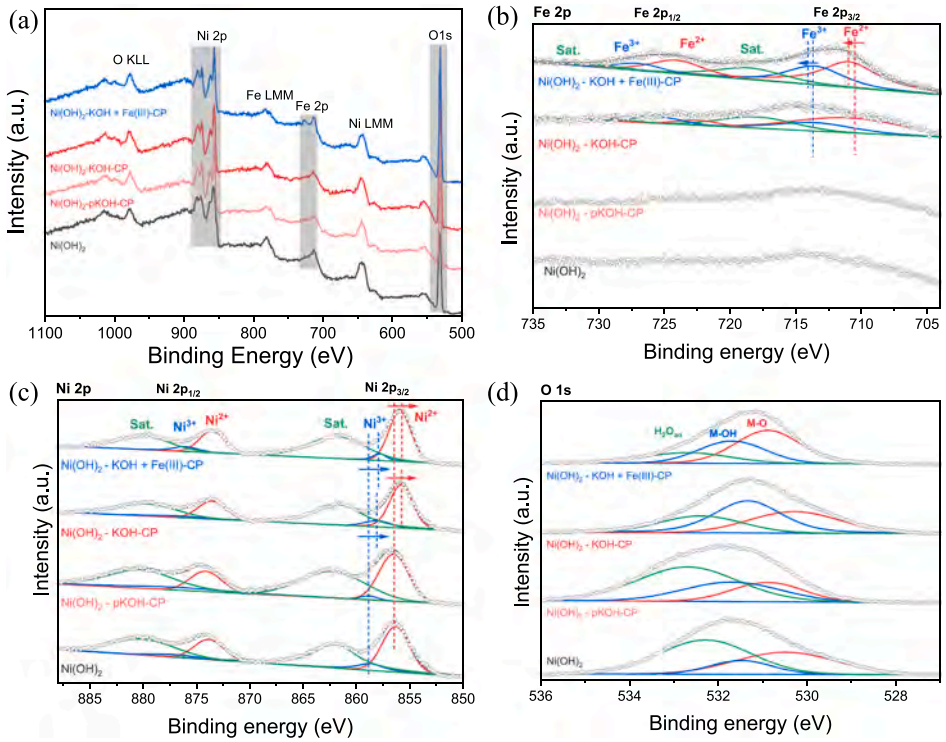

Fig. 5. (a) XPS survey, (b) XPS Fe 2p, (c) XPS Ni 2p, and (d) XPS O 1 s spectra of the $Ni(OH)_2$, $Ni(OH)_2$ after CP test for 50 h in pKOH and KOH as well as CP test for 50 h in KOH + Fe(III).

are NiOOH and FeOOH. The high-angle annular dark-field scanning TEM (HAADF-STEM) (Fig. 4**d**) and the EDS analysis (Fig. 4**e-4 h**) of the sample demonstrates the uniform dispersion of Fe, Ni and O. The EDS maps of the sample obtained from the SEM equipped with the EDS detector also show uniform distributions of Fe, Ni and O in both the nanosheet and nanofusiform structure (**Fig. S12**), indicating that the *in situ* formed NiOOH is doped with Fe (Fe-NiOOH) and FeOOH is doped with Ni (Ni-FeOOH). The *in situ* EIS analysis was conducted at various potentials on the $Ni(OH)_2$ electrode and Fe-NiOOH/Ni-FeOOH containing $Ni(OH)_2$ electrode in KOH + Fe(III) solution to determine the effect of the bimetallic interfaces on the reaction kinetics. Before the EIS measurements, the $Ni(OH)_2$ electrode performed CP testing for 50 h to form the constructed interface (Fe-NiOOH/Ni-FeOOH). The Bode phase diagram of the Fe-NiOOH/Ni-FeOOH contained electrode shows the same inflection points at 1.5 V in the low-frequency region as that of the $Ni(OH)_2$ electrode in KOH + Fe(III) (**Fig. S13a and S13b**), which are consistent with the OER activity in Fig. 3**c**. Meanwhile, the phase angle value and the charge transfer resistance (**Fig. S13c and S13d**) of the electrode with Fe-NiOOH/Ni-FeOOH interfaces are similar with that of the $Ni(OH)_2$ electrode in KOH + Fe(III), which further indicates that the

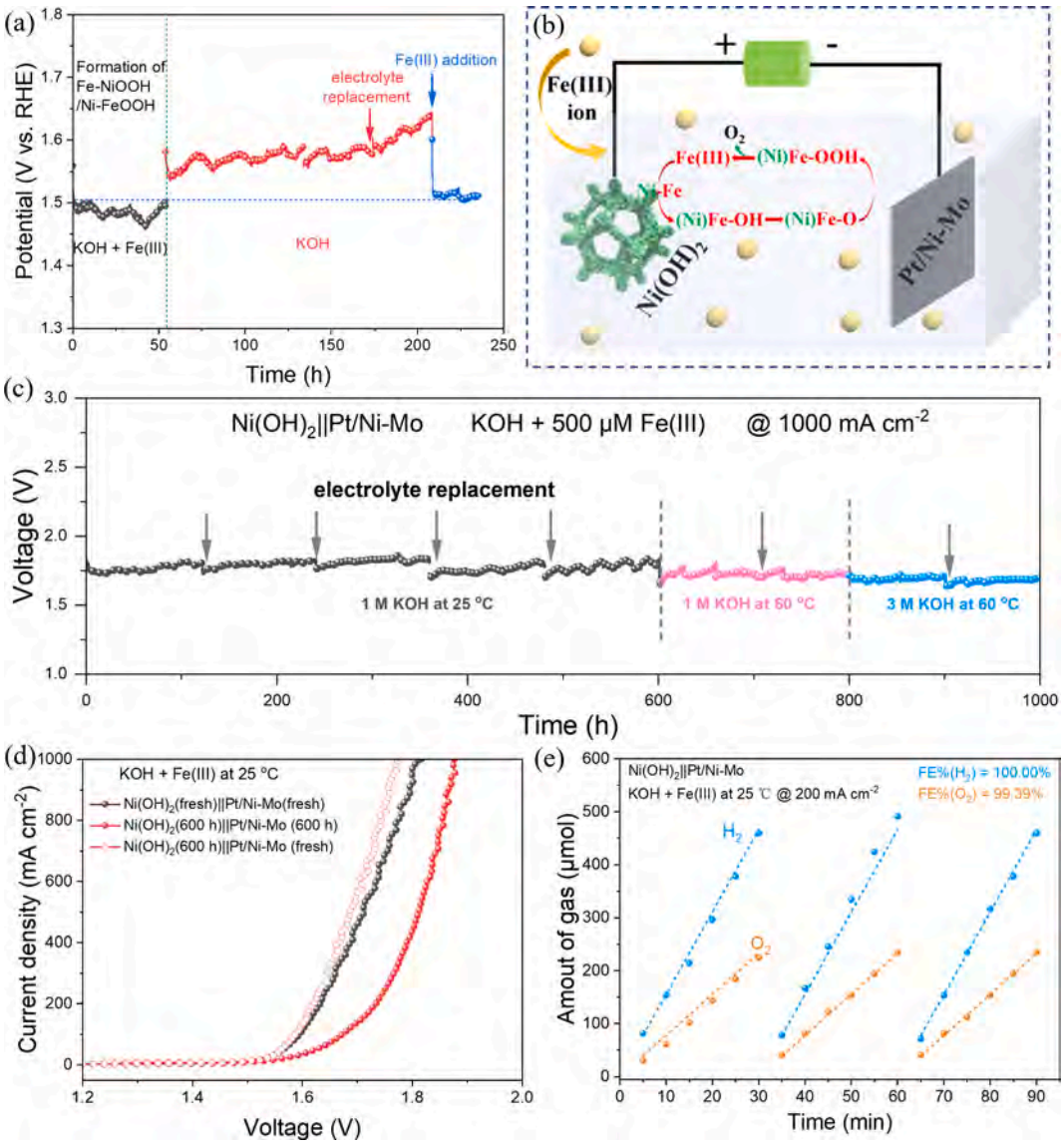

Fig. 6. (a) CP plots of the $Ni(OH)_2$ in KOH + Fe(III) for 50 h and then in KOH for 150 h, followed by another 24 h after adding Fe(III) to KOH; (b) Proposed Fe ion-catalyzed mechanism of OER in alkaline electrolyte on $Ni(OH)_2$ electrode; (c) Long-term stability test of the two-electrode system with the $Ni(OH)_2$ as the anode and Pt/Ni-Mo as the cathode in 1/3 M KOH containing 500 μM Fe(III) at 25/60 °C at a current density of 1,000 mA cm^{-2}; (d) LSV curves before and after the stability test in KOH + Fe(III) at 25 °C; (e) Faradaic efficiency of the $Ni(OH)_2$||Pt/Ni-Mo in KOH + Fe(III) at 25 °C at a current density of 200 mA cm^{-2}.

Fe(III) ions play the main role in improving the reaction kinetics.

The surface environment and valence states of the samples were further analyzed by XPS, involving the sample of pristine $Ni(OH)_2$, the $Ni(OH)_2$ after CP test for 50 h in pKOH, KOH, and KOH + Fe(III). In the survey spectra, all the samples exhibit the presence of Ni and O elements, while the Fe element only occurs on the samples after 50 h-tested in KOH and KOH + Fe(III) (Fig. 5**a**). In the fine Fe 2p spectra, the sample of 50 h-tested in KOH also shows the Fe composition, which should be stemmed from the Fe impurity in KOH. In Fe 2p spectra, four pairs of peaks are fitted, in which the binding energies at 712.3 and 725.8 eV are assigned to Fe^{3+} species and those 710.2 and 723.8 eV originate from Fe^{2+} species (Fig. 5**b**) [55]. The Fe^{2+} and Fe^{3+} peaks in the Fe $2p_{3/2}$ region both shift to higher binding energy of the sample in KOH + Fe (III), which implies the generation of Fe species with high oxidation state. In Ni 2p spectra, the fitting peak at 858.8 and 877.3 eV are characteristic of Ni^{3+} and those at 856.4 and 873.9 eV correspond to Ni^{2+} (Fig. 5**c**) [56]. For the sample after testing in Fe(III)-containing electrolyte, the Ni^{2+} and Ni^{3+} in Ni $2p_{3/2}$ region both shift to lower binding energy, indicating that Fe(III) incorporation endows the Ni on the surface with electron-rich state favoring the pre-oxidation of Ni species and promoting the OER activity. The opposite binding energy shift of Fe 2p and Ni 2p peak reveals the electronic interaction between Fe and Ni. The O 1 s spectra in Fig. 5**d** present three binding energies at 530.4, 531.5, and 532.3 eV, which are ascribed to the lattice of oxides, hydroxides, and absorbed water, respectively [57]. The compositions of the samples were further investigated by *ex situ* Raman spectra on pristine $Ni(OH)_2$, and $Ni(OH)_2$ after LSV and CP testing in KOH and KOH + Fe(III). As shown in **Fig. S14**, the peaks of Ni^{III}-O ascribed to NiOOH exist on all the samples except pristine $Ni(OH)_2$ [52,53]. The intensity of Ni^{III}-O is more larger in the sample after testing in Fe(III) containing electrolyte, implying that Fe(III) promote the generation of intermediate. However, the peak of Fe-O only appears on the sample after CP testing in KOH + Fe(III) [40,49,58], indicating the FeOOH intermediate can only generate in the Fe(III) containing environment.

Based on the above results, the Fe-NiOOH/Ni-FeOOH interfaces are totally formed *in situ* after the 50-h CP measurement. The OER activity and the corresponding C_{dl} values do not change with different CP testing time (Fig. 3**c and 3d**), which demonstrates that maybe the Fe-NiOOH/

Ni-FeOOH structure forms *in situ* even after a LSV test with a short testing time. Moreover, the pH dependence of $Ni(OH)_2$ in KOH + Fe(III) was performed to examine the OER mechanism (**Fig. S15**). The parallel Nernst shifts (the inset of **Fig. S15a**) of the polarization curves can be observed under different pH values of 13.15, 13.44, 13.55, and 13.71 indicating one H^+/OH^- per electron transfer [59]. By plotting the potential versus pH values at the current density of 5 mA cm^{-2}, the current density selected to alleviate the influence of electrochemical polarization under high current density, a 57.8 mV/pH potential shift was obtained (**Fig. S15b**), which is very close to the theoretical value of AEM (59.1 mV/pH) [60]. Taking the above results into account, Fe(III) promotes the OER kinetics by the cyclical formation of intermediates (Fe(III) → (Ni)Fe^{x+} → (Ni)Fe-OH → (Ni)Fe-O → (Ni)Fe-OOH → Fe(III) (+O_2)) on the electrode/electrolyte interface, and thus, the constant Fe(III)-containing environment is vital to maintaining the stability of the system. As shown in Fig. 6**a**, the $Ni(OH)_2$ electrode is first tested for 50 h in KOH + Fe(III) for the generation of Fe-NiOOH/Ni-FeOOH structures, during which the electrode shows no obvious degradation on OER activity. After that, the Fe-NiOOH/Ni-FeOOH contained electrode was immersed in deionized water for 5 h to eliminate the absorbed Fe(III) and then tested in fresh KOH, and the results show that the OER activity of the cleaned electrode gradually decreases with testing time. Interestingly, the oxidation potential immediately plummet to the initial value after addition of Fe(III) to the alkaline electrolyte, indicating that OER activity recovers to the original excellent level. The LSV curves (**Fig. S16**) corresponding to the same stage in Fig. 6**a** demonstrate the same phenomenon. All the above results suggest that although some Fe-NiOOH/Ni-FeOOH form *in situ* in the system, the availability of Fe(III) in the alkaline electrolyte is critical to maintain the OER efficiency via cyclical evolution of (Ni)Fe-based intermediate. The well agreed OER mechanism for transition metal-based catalysts is the adsorbate evolution mechanism (AEM), where the active site M of a (pre)catalyst experiences evolution of M → M−OH → M−O → M−OOH → M to emit O_2 and OER cycling occurs no matter what the starting (pre)catalyst is. Hence, according to the AEM mechanism, we hypothesize that the OER process is Fe^{3+} → (Ni)Fe^{x+} → (Ni)Fe-OH → (Ni)Fe-O → (Ni)Fe-OOH → Fe^{3+} on the electrodes to release O_2 as shown in Fig. 6**b**.

3.3. The water splitting system with Fe(III) availability

For industrial applications, the large current density (1000 mAcm^{-2}-level) and long-term stability (over 1000 h), especially at low overpotentials (<300 mV), are critical standards, which means a high rate of hydrogen production [61,62]. To demonstrate the feasibility of Fe(III)-catalyzed system for electrochemical water splitting under high current density, the electrolyzer was constructed with $Ni(OH)_2$ electrode as anode and Pt/Ni-Mo electrode as cathode in the 500 μM Fe(III)-containing alkaline electrolyte (Fig. 6**b**). The electrolyte was operated in KOH electrolyte with different concentration (1 M and 3 M) and at different temperature (25 and 60 °C) to simulate the industrial conditions. **Fig. S17** shows the LSV curves (without *i*R compensation) of the electrolyzer in different operating conditions, including 1 M KOH with 500 μM Fe(III) at 25/60 °C and 3 M KOH with 500 μM Fe(III) at 25/60 °C. The long-time stability under high current density of 1000 mA cm^{-2} is shown in Fig. 6**c**. Tested in 1 M KOH at 25 °C for 600 h, the system only exhibits negligible potential increase. As the real concentration of Fe(III) ions possibly decreases with time due to the *in situ* construction of Fe-NiOOH/Ni-FeOOH interfaces on the surface of the electrode and the colloidal formation of $Fe(OH)_3$ in the alkaline electrolyte, the alkaline solution with Fe (III) addition need to be replaced regularly. By replacing the Fe(III)-containing electrolyte every 120 h, the performance can return to the original level. Fig. 6**d** compares the LSV curve before and after 600-h test. The water splitting activity of the electrolyzer shows obvious decay after reaction but can recover by replacing the Pt/Ni-Mo cathode with a new one. The results indicate that the slightly increasing potential in Fig. 6**c** might be due to the deterioration of the cathode or the formation and release of gas bubbles. The $Ni(OH)_2$ after testing for 600 h exhibits the similar nanosheet and nanofusiform materials as that of 50 h (Fig. 3**g, 3 h, and S10**). The system operated in Fe(III) containing 1 M KOH and 3 M KOH at 60 °C also exhibits the robust stability for 200 h respectively (Fig. 6**c and S18**).

The Faradaic efficiency (FE) is an important parameter to evaluate the efficiency for hydrogen and oxygen production in electrochemical water splitting system. FE of the $Ni(OH)_2$ involved electrolyzer for hydrogen and oxygen production catalyzed by Fe(III) is conducted at current densities of 100 and 200 mA cm^{-2} (Fig. 6**e** and **Fig. S19**) for three parallel tests. The FE for hydrogen production at 100 and 200 mA cm^{-2} are both about 100 %, whereas the FE for oxygen production increases from about 97.05 % at 100 mA cm^{-2} to about 99.39 % at 200 mA cm^{-2}. The phenomenon might be due to that the *in situ* formation of nanofusiform material Ni-FeOOH requires some applied electricity. With the current density increasing, the ratio of electricity to generate Ni-FeOOH is relatively low, thus producing a larger FE.

4. Conclusions

A simple, cost-effective, and efficient strategy to enhance the OER performance is described. The $Ni(OH)_2$ nanosheet arrays electrode shows significantly boosted OER activity and dynamical stability when Fe(III) is added to the KOH solution. The electrochemical analysis and structure characterization are performed to investigate the catalysis effect of Fe(III). The results indicate that Fe(III) not only enhances the reaction kinetics, but also serves as active sites via the cyclical generation of intermediate Fe(III) → (Ni)Fe^{x+} → (Ni)Fe-OH → (Ni)Fe-O → (Ni)Fe-OOH → Fe(III) to emit O_2, and the Fe-NiOOH/Ni-FeOOH interfaces forms *in situ* on the surface of $Ni(OH)_2$ electrode. The Fe(III)-catalyzed water-splitting system exhibits robust stability at large current densities. Under industrial conditions, degradation during the reaction can be recovered by replacing the Fe(III) containing electrolytes. This study reveals a new perspective in the design of efficient and stable water splitting systems for commercial applications.

Declaration of Competing Interest

The authors declare that they have no known competing financial interests or personal relationships that could have appeared to influence the work reported in this paper.

Data availability

Data will be made available on request.

Acknowledgement

This work was financially supported by the Special Fund Project for Science and Technology Innovation Strategy of Guangdong Province (Grant No. STKJ202209077 and STKJ202209083), the Guangdong Province Universities and Colleges Pearl River Scholar Funded Scheme 2019 (GDUPS2019), and City University of Hong Kong Strategic Research Grant (SRG) (Grant No. 7005505).

Appendix A. Supplementary data

Supplementary data to this article can be found online at https://doi.org/10.1016/j.cej.2023.147155.

References

[1] X. Peng, S. Xie, S. Xiong, R. Li, P. Wang, X. Zhang, Z. Liu, L. Hu, B. Gao, P. Kelly, Ultralow-voltage hydrogen production and simultaneous Rhodamine B beneficiation in neutral wastewater, J. Energy Chem. 81 (2023) 574–582, https://doi.org/10.1016/j.jechem.2023.03.022.

[2] K. Chen, Y.-H. Cao, S. Yadav, G.-C. Kim, Z. Han, W. Wang, W.-J. Zhang, V. Dao, I.-H. Lee, Electronic structure reconfiguration of nickel–cobalt layered double hydroxide nanoflakes via engineered heteroatom and oxygen-vacancies defect for efficient electrochemical water splitting, Chem. Eng. J. 463 (2023), 142396. https://www.sciencedirect.com/science/article/pii/S1385894723011270.

[3] J. Zhu, L. Hu, P. Zhao, L.Y.S. Lee, K.-Y. Wong, Recent advances in electrocatalytic hydrogen evolution using nanoparticles, Chem. Rev. 120 (2020) 851–918, https://doi.org/10.1021/acs.chemrev.9b00248.

[4] M. Rafiq, X. Hu, Z. Ye, A. Qayum, H. Xia, L. Hu, F. Lu, P.K. Chu, Recent advances in structural engineering of 2D hexagonal boron nitride electrocatalysts, Nano Energy 91 (2022), 106661. https://www.sciencedirect.com/science/article/pii/S2211285521009125.

[5] Y. Zhu, H.A. Tahini, Z. Hu, Z.-G. Chen, W. Zhou, A.C. Komarek, Q. Lin, H.-J. Lin, C.-T. Chen, Y. Zhong, M.T. Fernández-Díaz, S.C. Smith, H. Wang, M. Liu, Z. Shao, Boosting oxygen evolution reaction by creating both metal ion and lattice-oxygen active sites in a complex oxide, Adv. Mater. 32 (2020) 1905025, https://doi.org/10.1002/adma.201905025.

[6] J. Zhou, L. Zhang, Y.-C. Huang, C.-L. Dong, H.-J. Lin, C.-T. Chen, L.H. Tjeng, Z. Hu, Voltage- and time-dependent valence state transition in cobalt oxide catalysts during the oxygen evolution reaction, Nat. Commun. 11 (2020) 1984, https://doi.org/10.1038/s41467-020-15925-2.

[7] B. Weng, F. Xu, C. Wang, W. Meng, C.R. Grice, Y. Yan, A layered $Na_{1-x}Ni_yFe_{1-y}O_2$ double oxide oxygen evolution reaction electrocatalyst for highly efficient water-splitting, Energ. Environ. Sci. 10 (2017) 121–128, https://doi.org/10.1039/C6EE03088B.

[8] Y.J. Son, K. Kawashima, B.R. Wygant, C.H. Lam, J.N. Burrow, H. Celio, A. Dolocan, J.G. Ekerdt, C.B. Mullins, Anodized nickel foam for oxygen evolution reaction in Fe-free and unpurified alkaline electrolytes at high current densities, ACS Nano 15 (2021) 3468–3480, https://doi.org/10.1021/acsnano.0c10788.

[9] C. Feng, F. Wang, Z. Liu, M. Nakabayashi, Y. Xiao, Q. Zeng, J. Fu, Q. Wu, C. Cui, Y. Han, A self-healing catalyst for electrocatalytic and photoelectrochemical oxygen evolution in highly alkaline conditions, Nat. Commun. 12 (2021) 1–10, https://doi.org/10.1038/s41467-021-26281-0.

[10] R. Gao, D. Yan, Recent development of Ni/Fe-based micro/nanostructures toward photo/electrochemical water oxidation, Adv. Energy Mater. 10 (2020) 1900954, https://doi.org/10.1002/aenm.201900954.

[11] X. Yu, P. Yang, S. Chen, M. Zhang, G. Shi, NiFe alloy protected silicon photoanode for efficient water splitting, Adv. Energy Mater. 7 (2017) 1601805, https://doi.org/10.1002/aenm.201601805.

[12] A. Qayum, X. Peng, J. Yuan, Y. Qu, J. Zhou, Z. Huang, H. Xia, Z. Liu, D.Q. Tan, P. K. Chu, Highly durable and efficient Ni-FeO_x/$FeNi_3$ electrocatalysts synthesized by a facile in situ combustion-based method for overall water splitting with large current densities, ACS Appl. Mater. Interfaces 14 (2022) 27842–27853, https://doi.org/10.1021/acsami.2c04562.

[13] Y. Liao, R. He, W. Pan, Y. Li, Y. Wang, J. Li, Y. Li, Lattice distortion induced Ce-doped NiFe-LDH for efficient oxygen evolution, Chem. Eng. J. 464 (2023), 142669. https://www.sciencedirect.com/science/article/pii/S1385894723014006.

[14] J. Peng, K. Peng, Rational design of amorphous NiFe-LDH/Co_3O_4–P heterostructure bifunctional electrocatalysts for overall water splitting, Mater. Chem. Phys. 297 (2023), 127412. https://www.sciencedirect.com/science/article/pii/S0254058423001207.

[15] Z. Li, M. Liu, J. Yan, L.Y.S. Lee, A "doping–interfacing" strategy enables efficient alkaline freshwater and seawater oxidation by NiFe-layered double hydroxides, Chem. Eng. J. 473 (2023), 145293. https://www.sciencedirect.com/science/article/pii/S138589472304024X.

[16] L. Hu, X. Zeng, X. Wei, H. Wang, Y. Wu, W. Gu, L. Shi, C. Zhu, Interface engineering for enhancing electrocatalytic oxygen evolution of NiFe LDH/NiTe heterostructures, Appl. Catal. B Environ. 273 (2020), 119014. https://www.sciencedirect.com/science/article/pii/S092633732030429X.

[17] Y. Wang, S. Tao, H. Lin, G. Wang, K. Zhao, R. Cai, K. Tao, C. Zhang, M. Sun, J. Hu, B. Huang, S. Yang, Atomically targeting NiFe LDH to create multivacancies for OER catalysis with a small organic anchor, Nano Energy 81 (2021), 105606. https://www.sciencedirect.com/science/article/pii/S2211285520311794.

[18] Y. Li, L. Hu, W. Zheng, X. Peng, M. Liu, P. Chu, L. Lee, Ni/Co-based nanosheet arrays for efficient oxygen evolution reaction, Nano Energy 52 (2018) 360–368. https://www.sciencedirect.com/science/article/pii/S221128551830572X.

[19] J. Zhang, J. Liu, L. Xi, Y. Yu, N. Chen, S. Sun, W. Wang, K.M. Lange, B. Zhang, Single-atom Au/NiFe layered double hydroxide electrocatalyst: probing the origin of activity for oxygen evolution reaction, J. Am. Chem. Soc. 140 (2018) 3876–3879, https://doi.org/10.1021/jacs.8b00752.

[20] H. Zhou, F. Yu, J. Sun, R. He, S. Chen, C.-W. Chu, Z. Ren, Highly active catalyst derived from a 3D foam of $Fe(PO_3)_2$/Ni_2P for extremely efficient water oxidation, P. Natl. A. Sci. 114 (2017) 5607–5611, https://doi.org/10.1073/pnas.1701562114.

[21] R.D.L. Smith, M.S. Prévot, R.D. Fagan, Z. Zhang, P.A. Sedach, M.K.J. Siu, S. Trudel, C.P. Berlinguette, Photochemical route for accessing amorphous metal oxide materials for water oxidation catalysis, Science 340 (2013) 60–63, https://doi.org/10.1126/science.1233638.

[22] H. Zhou, F. Yu, Q. Zhu, J. Sun, F. Qin, L. Yu, J. Bao, Y. Yu, S. Chen, Z. Ren, Water splitting by electrolysis at high current densities under 1.6 volts, Energ. Environ. Sci. 11 (2018) 2858–2864, https://doi.org/10.1039/C8EE00927A.

[23] Z. Huang, S. Zhu, Y. Duan, C. Pi, X. Zhang, A. Reda Woldu, J-X. Jian, P.K. Chu, Q-X. Tong, L. Hu, X. Yao, Insights into ionic association boosting water oxidation activity and dynamic stability, J. Energy Chem. (2023), https://doi.org/10.1016/j.jechem.2023.10.036.

[24] M. Etzi Coller Pascuzzi, A.J.W. Man, A. Goryachev, J.P. Hofmann, E.J.M. Hensen, Investigation of the stability of NiFe-(oxy)hydroxide anodes in alkaline water electrolysis under industrially relevant conditions, Catal. Sci. Technol. 10 (2020) 5593–5601, https://doi.org/10.1039/D0CY01179G.

[25] S. Lee, H.-S. Cho, W.-C. Cho, S.-K. Kim, Y. Cho, C.-H. Kim, Operational durability of three-dimensional Ni-Fe layered double hydroxide electrocatalyst for water oxidation, Electrochim. Acta 315 (2019) 94–101. https://www.sciencedirect.com/science/article/pii/S0013468619310217.

[26] A. Moysiadou, X. Hu, Stability profiles of transition metal oxides in the oxygen evolution reaction in alkaline medium, J. Mater. Chem. A 7 (2019) 25865–25877, https://doi.org/10.1039/C9TA10308B.

[27] R. Chen, S.F. Hung, D. Zhou, J. Gao, C. Yang, H. Tao, H.B. Yang, L. Zhang, L. Zhang, Q. Xiong, Layered structure causes bulk NiFe layered double hydroxide unstable in alkaline oxygen evolution reaction, Adv. Mater. 31 (2019) 1903909, https://doi.org/10.1002/adma.201903909.

[28] L. Peng, N. Yang, Y. Yang, Q. Wang, X. Xie, D. Sun-Waterhouse, L. Shang, T. Zhang, G.I.N. Waterhouse, Atomic cation-vacancy engineering of NiFe-layered double hydroxides for improved activity and stability towards the oxygen evolution reaction, Angew. Chem. Int. Edit. 133 (2021) 24817–24824, https://doi.org/10.1002/ange.202109938.

[29] C. Kuai, Z. Xu, C. Xi, A. Hu, Z. Yang, Y. Zhang, C.-J. Sun, L. Li, D. Sokaras, C. Dong, Phase segregation reversibility in mixed-metal hydroxide water oxidation catalysts, Nat. Catal. 3 (2020) 743–753, https://doi.org/10.1038/s41929-020-0496-z.

[30] W.H. Lee, Y.-J. Ko, J.H. Kim, C.H. Choi, K.H. Chae, H. Kim, Y.J. Hwang, B.K. Min, P. Strasser, H.-S. Oh, High crystallinity design of Ir-based catalysts drives catalytic reversibility for water electrolysis and fuel cells, Nat. Commun. 12 (2021) 1–10, https://doi.org/10.1038/s41467-021-24578-8.

[31] D.A. Corrigan, The catalysis of the oxygen evolution reaction by iron impurities in thin film nickel oxide electrodes, J. Electrochem. Soc. 134 (1987) 377, https://doi.org/10.1149/1.2100463.

[32] L. Trotochaud, S.L. Young, J.K. Ranney, S.W. Boettcher, Nickel–iron oxyhydroxide oxygen-evolution electrocatalysts: the role of intentional and incidental iron incorporation, J. Am. Chem. Soc. 136 (2014) 6744–6753, https://doi.org/10.1021/ja502379c.

[33] S. Anantharaj, S. Kundu, S. Noda, "The Fe Effect": A review unveiling the critical roles of Fe in enhancing OER activity of Ni and Co based catalysts, Nano Energy 80 (2021), 105514, https://doi.org/10.1016/j.nanoen.2020.105514.

[34] D.Y. Chung, P.P. Lopes, Dynamic stability of active sites in hydr(oxy)oxides for the oxygen evolution reaction, Nat. Energy 5 (2020) 222–230, https://doi.org/10.1038/s41560-020-0576-y.

[35] J. Deng, M.R. Nellist, M.B. Stevens, C. Dette, Y. Wang, S.W. Boettcher, Morphology dynamics of single-layered $Ni(OH)_2$/NiOOH nanosheets and subsequent Fe incorporation studied by in situ electrochemical atomic force microscopy, Nano Lett. 17 (2017) 6922–6926, https://doi.org/10.1021/acs.nanolett.7b03313.

[36] R. Farhat, J. Dhainy, L.I. Halaoui, OER catalysis at activated and codeposited NiFe-Oxo/hydroxide thin films is due to postdeposition surface-Fe and is not sustainable without Fe in solution, ACS Catal. 10 (2020) 20–35, https://doi.org/10.1021/acscatal.9b02580.

[37] J. Hao, J. Liu, D. Wu, M. Chen, Y. Liang, Q. Wang, L. Wang, X.-Z. Fu, J.-L. Luo, In situ facile fabrication of Ni(OH)2 nanosheet arrays for electrocatalytic co-production of formate and hydrogen from methanol in alkaline solution, Appl. Catal. B Environ. 281 (2021), 119510. https://www.sciencedirect.com/science/article/pii/S0926337320309255.

[38] F. Yang, Y. Luo, Q. Yu, Z. Zhang, S. Zhang, Z. Liu, W. Ren, H.-M. Cheng, J. Li, B. Liu, A durable and efficient electrocatalyst for saline water splitting with current density exceeding 2000 mA cm^{-2}, Adv. Funct. Mater. 31 (2021) 2010367, https://doi.org/10.1002/adfm.202010367.

[39] Z. Li, M. Shao, H. An, Z. Wang, S. Xu, M. Wei, D.G. Evans, X. Duan, Fast electrosynthesis of Fe-containing layered double hydroxide arrays toward highly efficient electrocatalytic oxidation reactions, Chem. Sci. 6 (2015) 6624–6631, https://doi.org/10.1039/C5SC02417J.

[40] J. Feng, M. Chen, P. Zhou, D. Liu, Y.-Y. Chen, B. He, H. Bai, D. Liu, W.F. Ip, S. Chen, D. Liu, W. Feng, J. Ni, H. Pan, Reconstruction optimization of distorted FeOOH/Ni hydroxide for enhanced oxygen evolution reaction, Mater. Today Energy 27 (2022), 101005. https://www.sciencedirect.com/science/article/pii/S2468606922000636.

[41] W. Chen, Y. Wang, B. Wu, J. Shi, Y. Li, L. Xu, C. Xie, W. Zhou, Y.-C. Huang, T. Wang, S. Du, M. Song, D. Wang, C. Chen, J. Zheng, J. Liu, C.-L. Dong, Y. Zou, J. Chen, S. Wang, Activated Ni–OH bonds in a catalyst facilitates the nucleophile oxidation reaction, Adv. Mater. 34 (2022) 2105320, https://doi.org/10.1002/adma.202105320.

[42] P. Zhou, X. Lv, S. Tao, J. Wu, H. Wang, X. Wei, T. Wang, B. Zhou, Y. Lu, T. Frauenheim, X. Fu, S. Wang, Y. Zou, Heterogeneous-interface-enhanced adsorption of organic and hydroxyl for biomass electrooxidation, Adv. Mater. 34 (2022) 2204089, https://doi.org/10.1002/adma.202204089.

[43] C. Chen, M. Sun, F. Zhang, H. Li, M. Sun, P. Fang, T. Song, W. Chen, J. Dong, B. Rosen, P. Chen, B. Huang, Y. Li, Adjacent Fe Site boosts electrocatalytic oxygen evolution at Co site in single-atom-catalyst through a dual-metal-site design, Energ. Environ. Sci. 16 (2023) 1685–1696, https://doi.org/10.1039/D2EE03930C.

[44] S. Wang, K. Zhao, Z. Chen, L. Wang, Z. Qi, J. Hao, W. Shi, New insights into cations effect in oxygen evolution reaction, Chem. Eng. J. 433 (2022), 133518. https://www.sciencedirect.com/science/article/pii/S1385894721050920.

[45] F. Bao, E. Kemppainen, I. Dorbandt, F. Xi, R. Bors, N. Maticiuc, R. Wenisch, R. Bagacki, C. Schary, U. Michalczik, P. Bogdanoff, I. Lauermann, R. van de Krol, R. Schlatmann, S. Calnan, Host, suppressor, and promoter—the roles of Ni and Fe on oxygen evolution reaction activity and stability of NiFe alloy thin films in

alkaline media, ACS Catal. 11 (2021) 10537–10552, https://doi.org/10.1021/acscatal.1c01190.
[46] H. Lei, L. Ma, Q. Wan, S. Tan, B. Yang, Z. Wang, W. Mai, H.J. Fan, Promoting surface reconstruction of NiFe layered double hydroxide for enhanced oxygen evolution, Adv. Energy Mater. 12 (2022) 2202522, https://doi.org/10.1002/aenm.202202522.
[47] Z. Qiu, C.-W. Tai, G.A. Niklasson, T. Edvinsson, Direct observation of active catalyst surface phases and the effect of dynamic self-optimization in NiFe-layered double hydroxides for alkaline water splitting, Energ. Environ. Sci. 12 (2019) 572–581, https://doi.org/10.1039/C8EE03282C.
[48] S. Lee, L. Bai, X. Hu, Deciphering iron-dependent activity in oxygen evolution catalyzed by nickel-iron layered double hydroxide, Angew. Chem. Int. Edit. 59 (2020) 8072–8077, https://doi.org/10.1002/anie.201915803.
[49] L. Bai, S. Lee, X. Hu, Spectroscopic and electrokinetic evidence for a bifunctional mechanism of the oxygen evolution reaction, Angew. Chem. Int. Edit. 60 (2021) 3095–3103, https://doi.org/10.1002/anie.202011388.
[50] K. Zhu, X. Zhu, W. Yang, Application of in situ techniques for the characterization of NiFe-based oxygen evolution reaction (OER) electrocatalysts, Angew. Chem. Int. Edit. 58 (2019) 1252–1265, https://doi.org/10.1002/anie.201802923.
[51] S. Klaus, Y. Cai, M.W. Louie, L. Trotochaud, A.T. Bell, Effects of Fe electrolyte impurities on $Ni(OH)_2$/NiOOH structure and oxygen evolution activity, J. Phys. Chem. C 119 (2015) 7243–7254, https://doi.org/10.1021/acs.jpcc.5b00105.
[52] P.W. Menezes, S. Yao, R. Beltrán-Suito, J.N. Hausmann, P.V. Menezes, M. Driess, Facile access to an active γ-NiOOH Electrocatalyst for durable water oxidation derived from an intermetallic nickel germanide precursor, Angew. Chem. Int. Edit. 60 (2021) 4640–4647, https://doi.org/10.1002/anie.202014331.
[53] P. Yan, Q. Liu, H. Zhang, L. Qiu, H.B. Wu, X.-Y. Yu, Deeply reconstructed hierarchical and defective NiOOH/FeOOH nanoboxes with accelerated kinetics for the oxygen evolution reaction, J. Mater. Chem. A 9 (2021) 15586–15594, https://doi.org/10.1039/D1TA03362J.
[54] R.-Y. Fan, J.-Y. Xie, H.-J. Liu, H.-Y. Wang, M.-X. Li, N. Yu, R.-N. Luan, Y.-M. Chai, B. Dong, Directional regulating dynamic equilibrium to continuously update electrocatalytic interface for oxygen evolution reaction, Chem. Eng. J. 431 (2022), 134040. https://www.sciencedirect.com/science/article/pii/S1385894721056151.
[55] Z. Wan, D. Yang, J. Chen, J. Tian, T.T. Isimjan, X. Yang, Oxygen-evolution catalysts based on iron-mediated nickel metal-organic frameworks, ACS Appl. Nano Mater. 2 (2019) 6334–6342, https://doi.org/10.1021/acsanm.9b01330.
[56] J. Chi, H. Yu, B. Qin, L. Fu, J. Jia, B. Yi, Z. Shao, Vertically aligned FeOOH/NiFe layered double hydroxides electrode for highly efficient oxygen evolution reaction, ACS Appl. Mater. Interfaces 9 (2017) 464–471, https://doi.org/10.1021/acsami.6b13360.
[57] G. Dong, M. Fang, J. Zhang, R. Wei, L. Shu, X. Liang, S. Yip, F. Wang, L. Guan, Z. Zheng, J.C. Ho, In situ formation of highly active Ni–Fe based oxygen-evolving electrocatalysts via simple reactive dip-coating, J. Mater. Chem. A 5 (2017) 11009–11015, https://doi.org/10.1039/C7TA01134B.
[58] D. Friebel, M.W. Louie, M. Bajdich, K.E. Sanwald, Y. Cai, A.M. Wise, M.-J. Cheng, D. Sokaras, T.-C. Weng, R. Alonso-Mori, R.C. Davis, J.R. Bargar, J.K. Nørskov, A. Nilsson, A.T. Bell, Identification of highly active Fe sites in (Ni, Fe)OOH for electrocatalytic water splitting, J. Am. Chem. Soc. 137 (2015) 1305–1313, https://doi.org/10.1021/ja511559d.
[59] D. Shi, Y. Ji, F. Lu, J. Yao, L. Pei, Construction of a NiFe-LDH catalyst with a three-dimensional unified gas diffusion layer structure via a facile acid etching route for the oxygen evolution reaction, Mater. Chem. Front. 7 (2023) 1335–1344, https://doi.org/10.1039/D2QM01300B.
[60] Y. Hao, Y. Li, J. Wu, L. Meng, J. Wang, C. Jia, T. Liu, X. Yang, Z.-P. Liu, M. Gong, Recognition of surface oxygen intermediates on NiFe oxyhydroxide oxygen-evolving catalysts by homogeneous oxidation reactivity, J. Am. Chem. Soc. 143 (2021) 1493–1502, https://doi.org/10.1021/jacs.0c11307.
[61] Q. Wen, Y. Zhao, Y. Liu, H. Li, T. Zhai, Ultrahigh-current-density and long-term-durability electrocatalysts for water splitting, Small 18 (2022) 2104513, https://doi.org/10.1002/smll.202104513.
[62] Y. Luo, Z. Zhang, M. Chhowalla, B. Liu, Recent advances in design of electrocatalysts for high-current-density water splitting, Adv. Mater. 34 (2022) 2108133, https://doi.org/10.1002/adma.202108133.

Supporting Information

Remarkably Boosted Water Oxidation Activity and Dynamic Stability at Large-Current–Density of $Ni(OH)_2$ Nanosheet Arrays by Fe Ion Association and Underlying Mechanism

Zanling Huang[a], Abebe Reda Woldu[a], Xiang Peng[c], Paul K. Chu[d], Qing-Xiao Tong[a*], and Liangsheng Hu[a,b*]

a Department of Chemistry and Key Laboratory for Preparation and Application of Ordered Structural Materials of Guangdong Province, Shantou University, Shantou, 515063, P. R. China

[b] Chemistry and Chemical Engineering Guangdong Laboratory, Shantou, 515063, P. R. China

[c] Hubei Key Laboratory of Plasma Chemistry and Advanced Materials, School of Materials Science and Engineering, Wuhan Institute of Technology, Wuhan, 430205, P. R. China

[d] Department of Physics, Department of Materials Science and Engineering, and Department of Biomedical Engineering, City University of Hong Kong, Tat Chee Avenue, Kowloon, Hong Kong, P. R. China

ORCID: 0000-0002-5581-4883 (P.K. Chu); 0000-0002-4133-2090 (L.S. Hu)

* Corresponding authors. qxtong@stu.edu.cn (Q.X. Tong), lshu@stu.edu.cn (L. S. Hu)

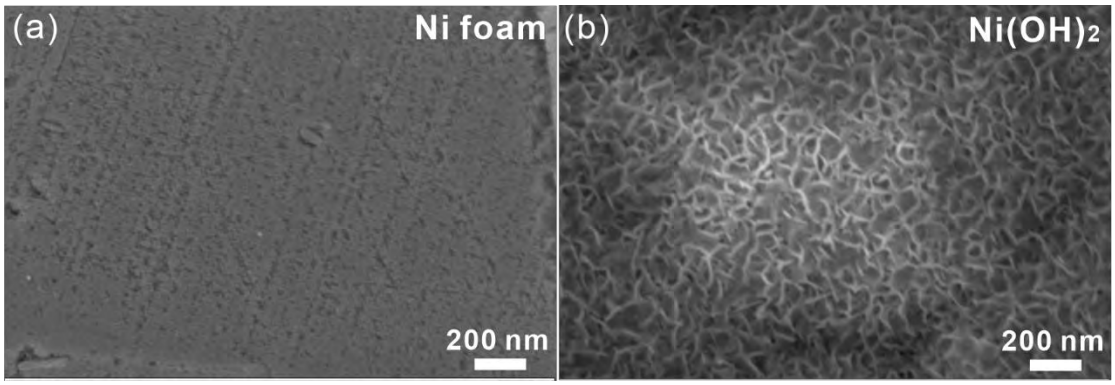

Fig. S1. SEM images of (a) Ni foam, (b) $Ni(OH)_2$.

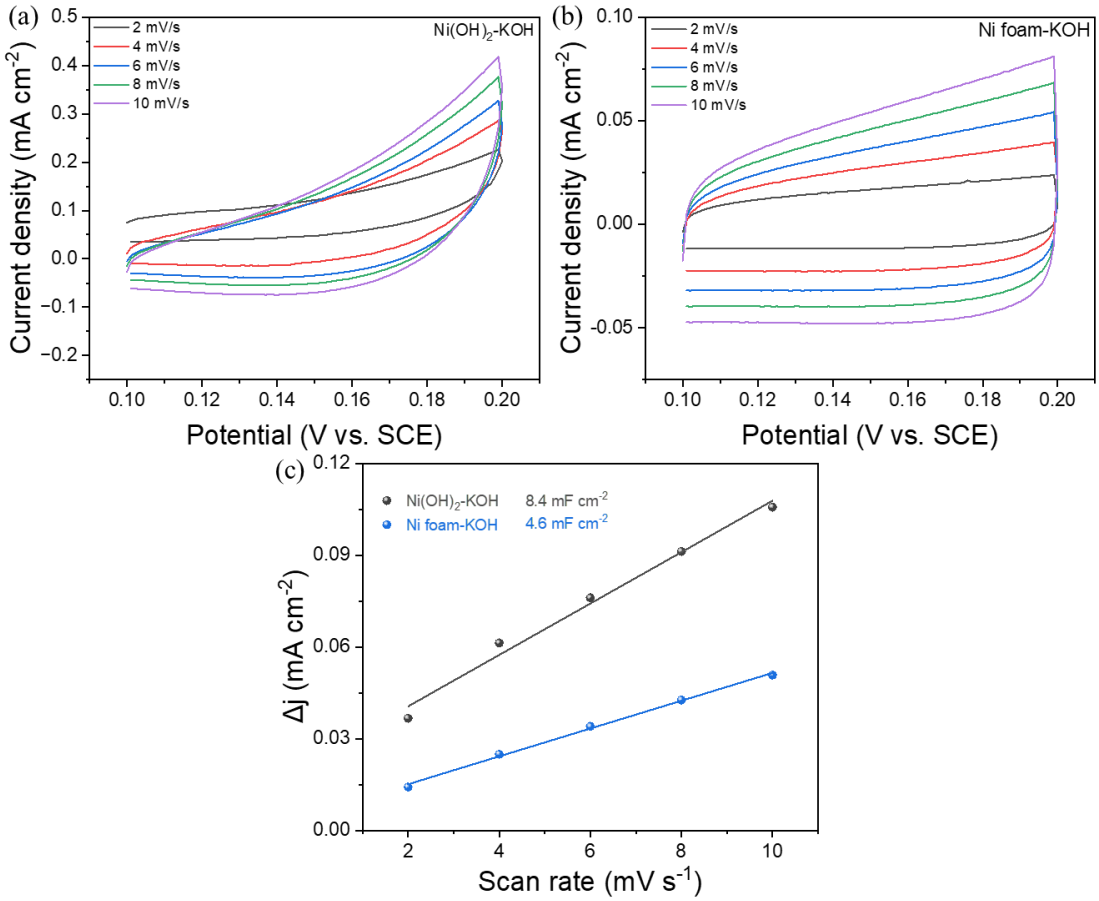

Fig. S2. The CV curves of (a) $Ni(OH)_2$, and (b) Ni foam in 1.0 M KOH, in the non-Faradaic range of 0.10-0.20 V with scanning rates of 2, 4, 6, 8, and 10 mV/s. (c) The corresponding C_{dl} values.

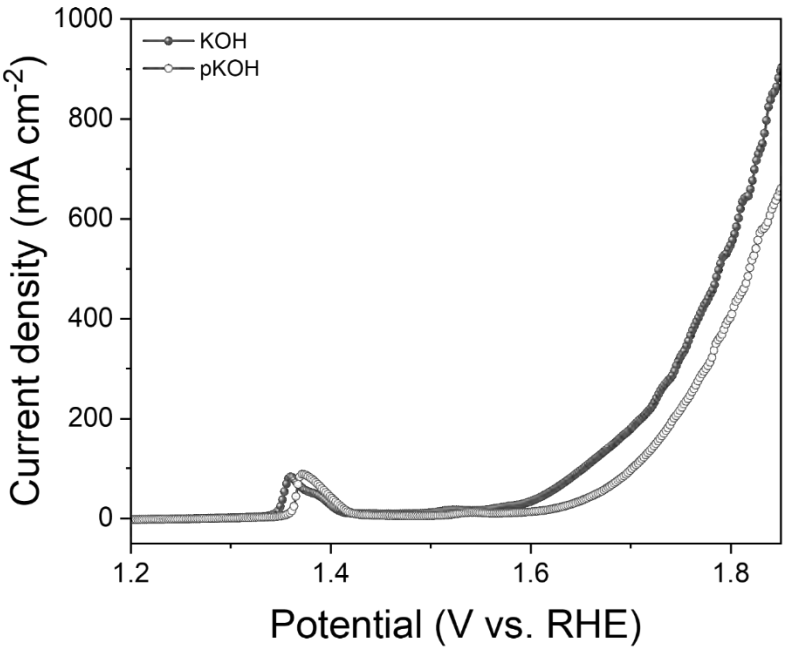

Fig. S3. The LSV curves of $Ni(OH)_2$ in KOH and pKOH.

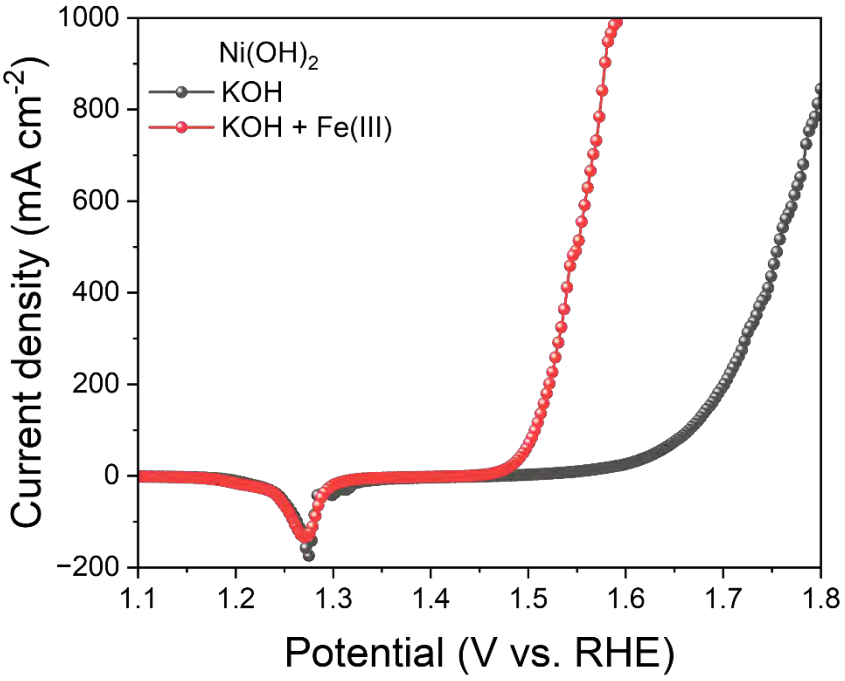

Fig. S4. The LSV curves of $Ni(OH)_2$ in KOH and KOH + Fe(III).

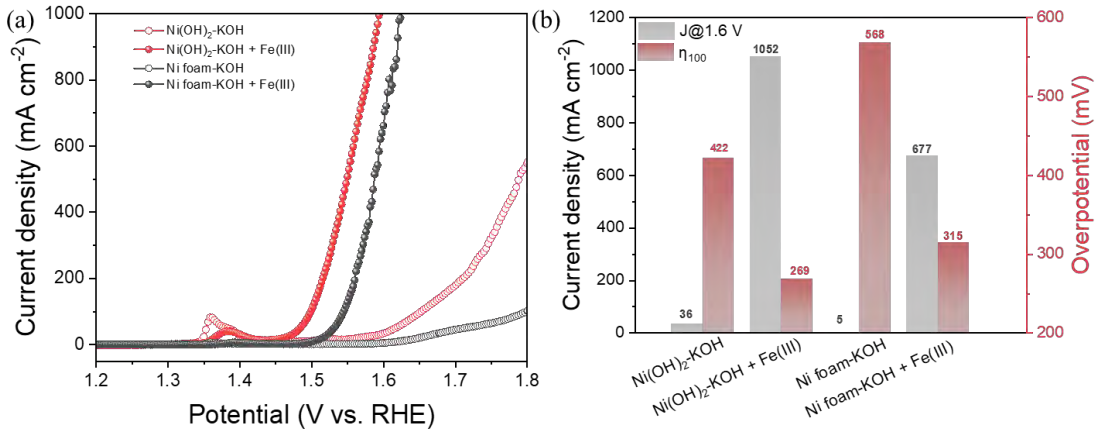

Fig. S5. (a) The LSV curves of $Ni(OH)_2$ and Ni foam in KOH and KOH + Fe(III); (b) Comparisons of J@1.6 V and η_{100} of $Ni(OH)_2$ and Ni foam in KOH and KOH + Fe(III).

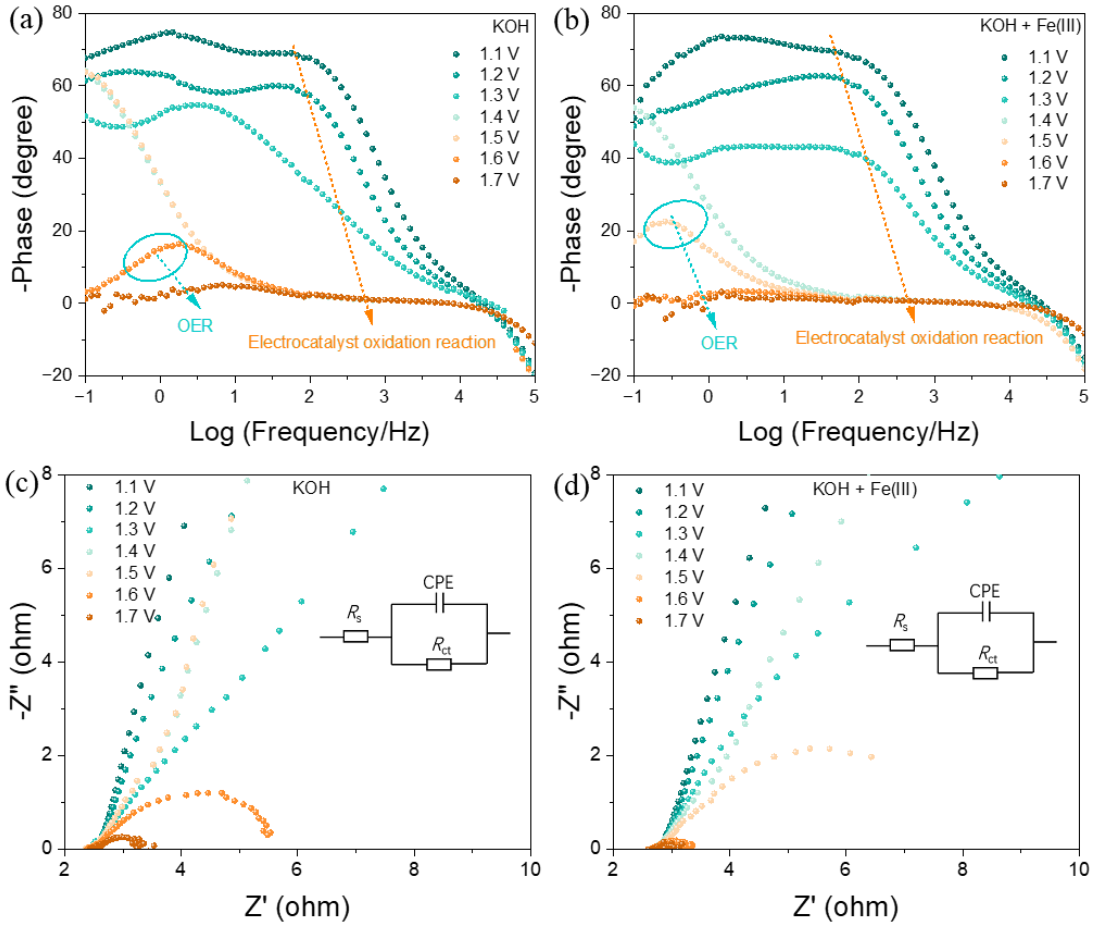

Fig. S6. (a, b) Bode-phase plots and (c, d) Nyquist plots of $Ni(OH)_2$ for different applied potentials in KOH and KOH + Fe(III), respectively.

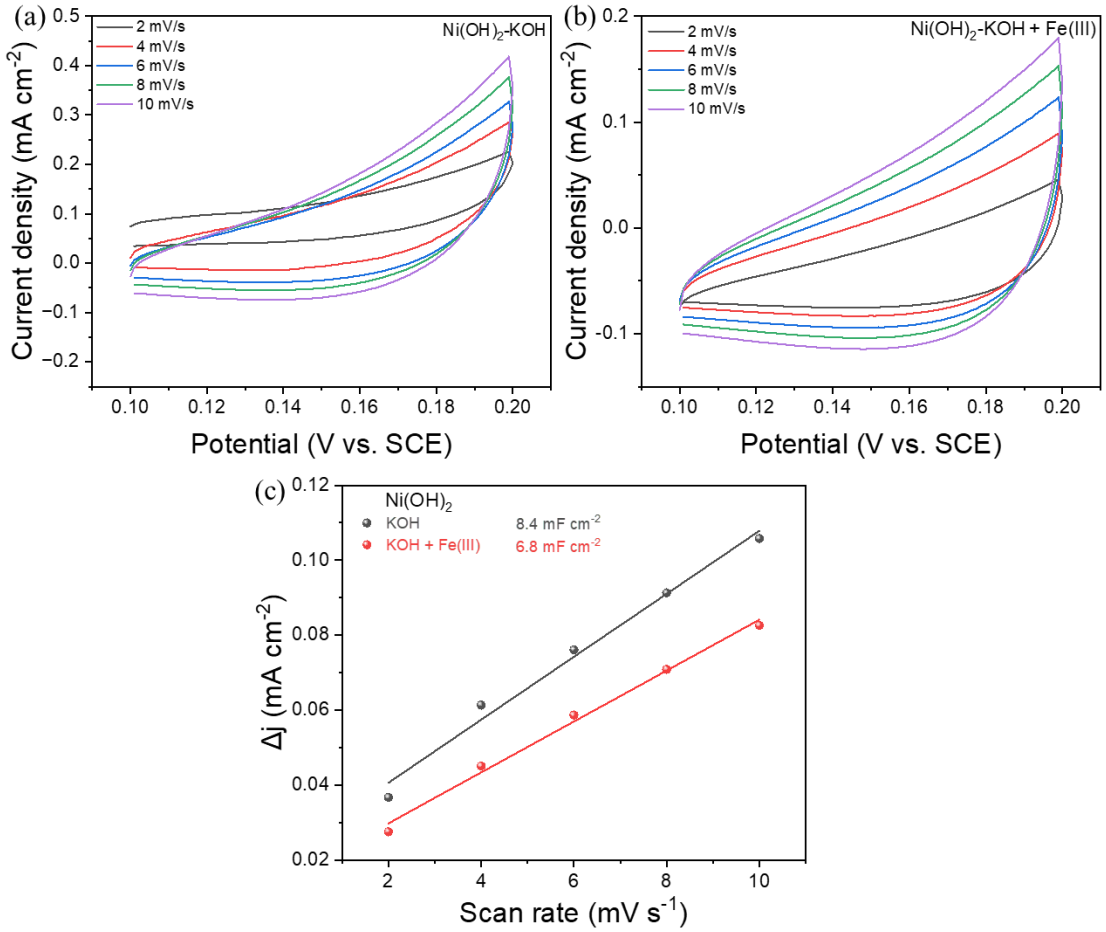

Fig. S7. The CV curves of $Ni(OH)_2$ in (a) KOH, and (b) KOH + Fe(III) in the non-Faradaic range of 0.10-0.20 V with scanning rates of 2, 4, 6, 8 and 10 mV/s. (c) The corresponding C_{dl} values.

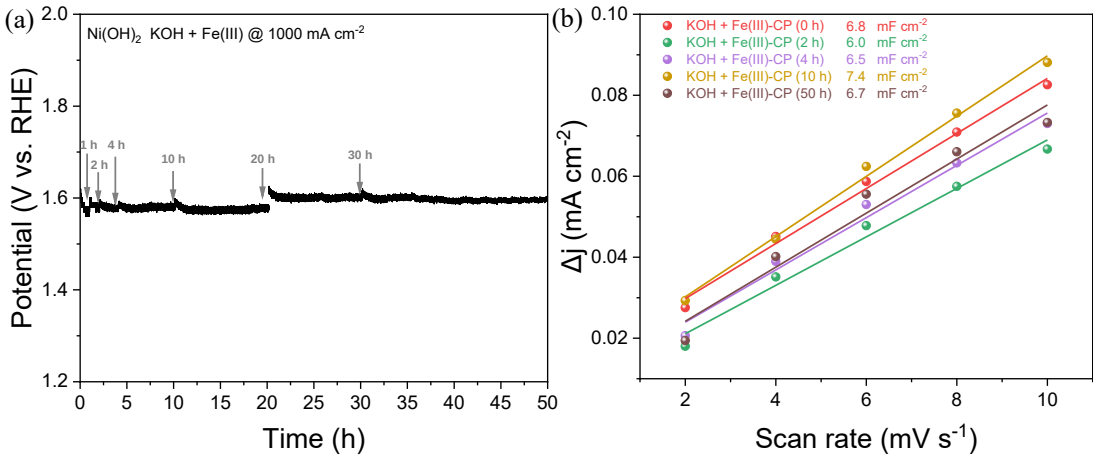

Fig. S8. (a) CP plot of $Ni(OH)_2$ in KOH + Fe(III); (b) The C_{dl} values of the $Ni(OH)_2$ obtained from KOH + Fe(III) after the CP test for different time (0, 2, 4, 10, 50 h).

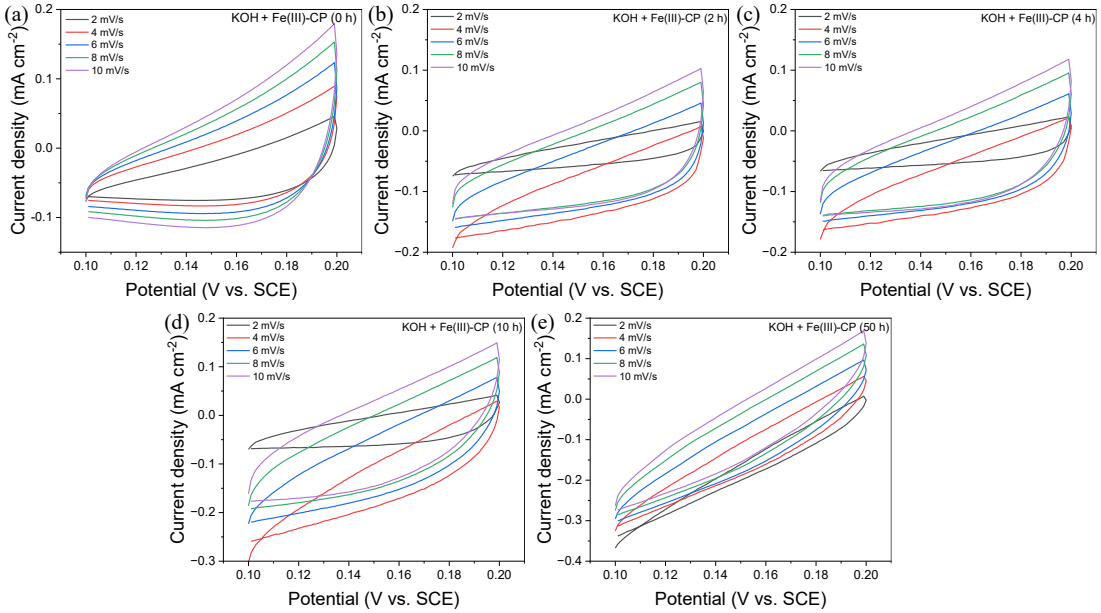

Fig. S9. The CV curves of $Ni(OH)_2$ in KOH + Fe(III) after CP testing in KOH + Fe(III) for (a) 0 h, (b) 2 h, (c) 4 h, (d) 10 h, and (e) 50 h in the non-Faradaic range of 0.10-0.20 V with scanning rates of 2, 4, 6, 8 and 10 mV/s.

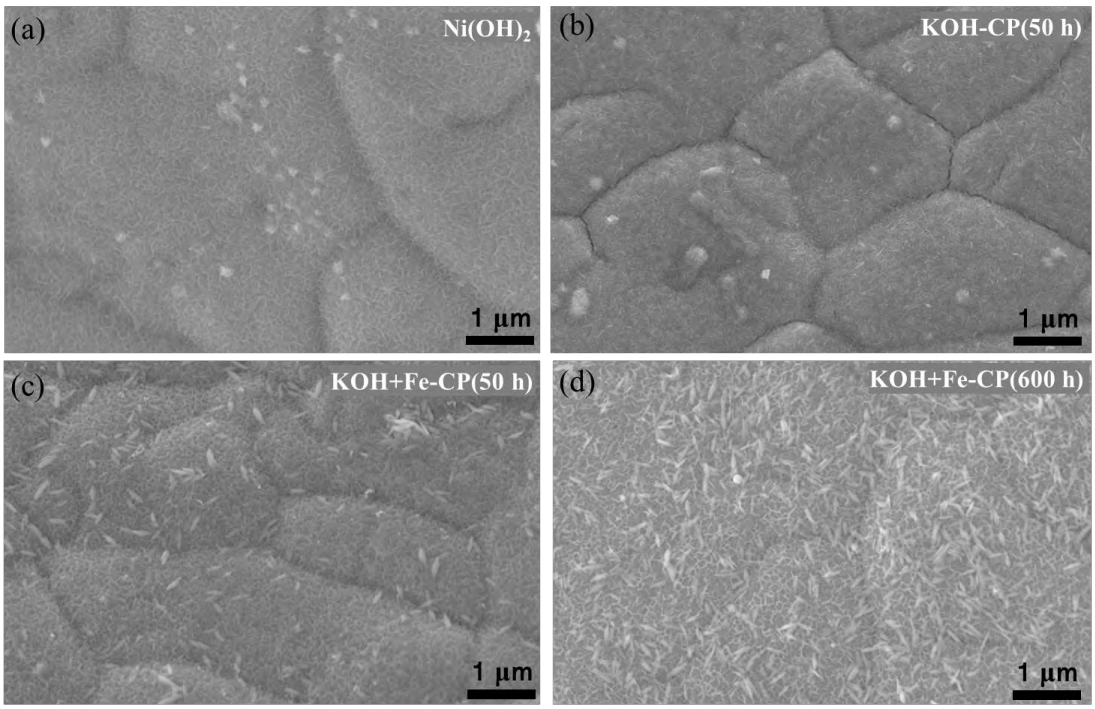

Fig. S10. Low-magnification SEM images of (a) $Ni(OH)_2$, $Ni(OH)_2$ after CP test for 50 h (b) in KOH, 50 h (c) and (d) 600 h in KOH + Fe(III).

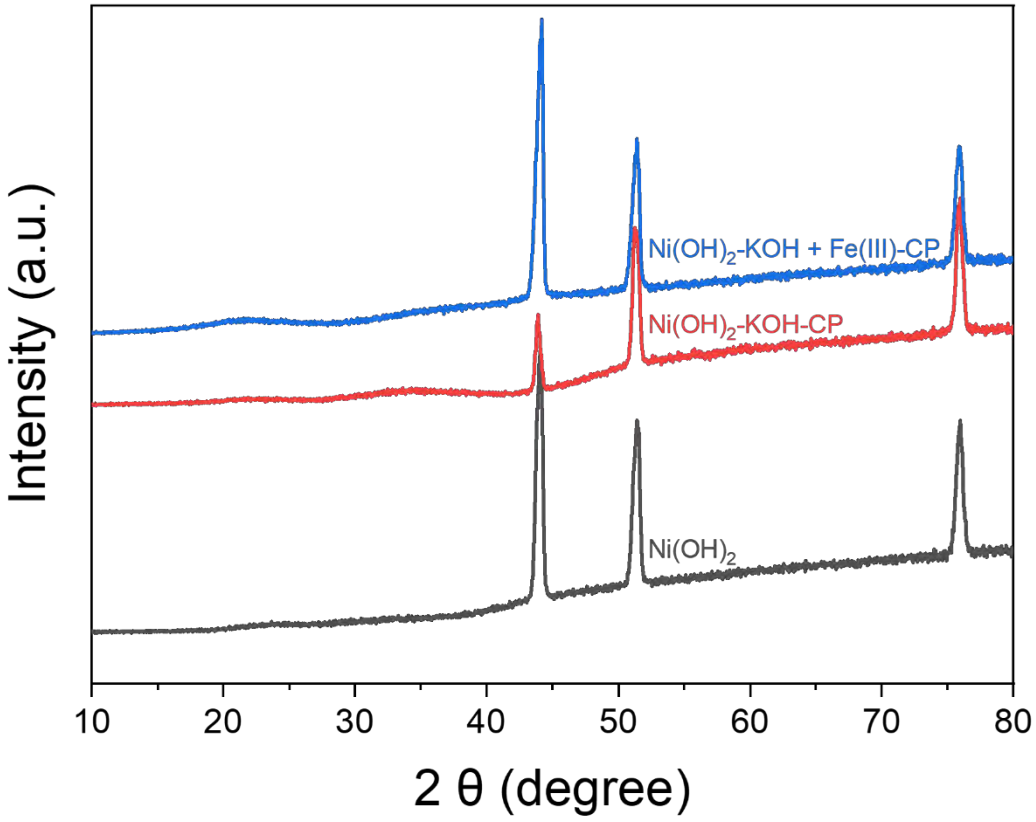

Fig. S11. XRD patterns of $Ni(OH)_2$, $Ni(OH)_2$ after the CP test for 50 h in KOH and KOH + Fe(III).

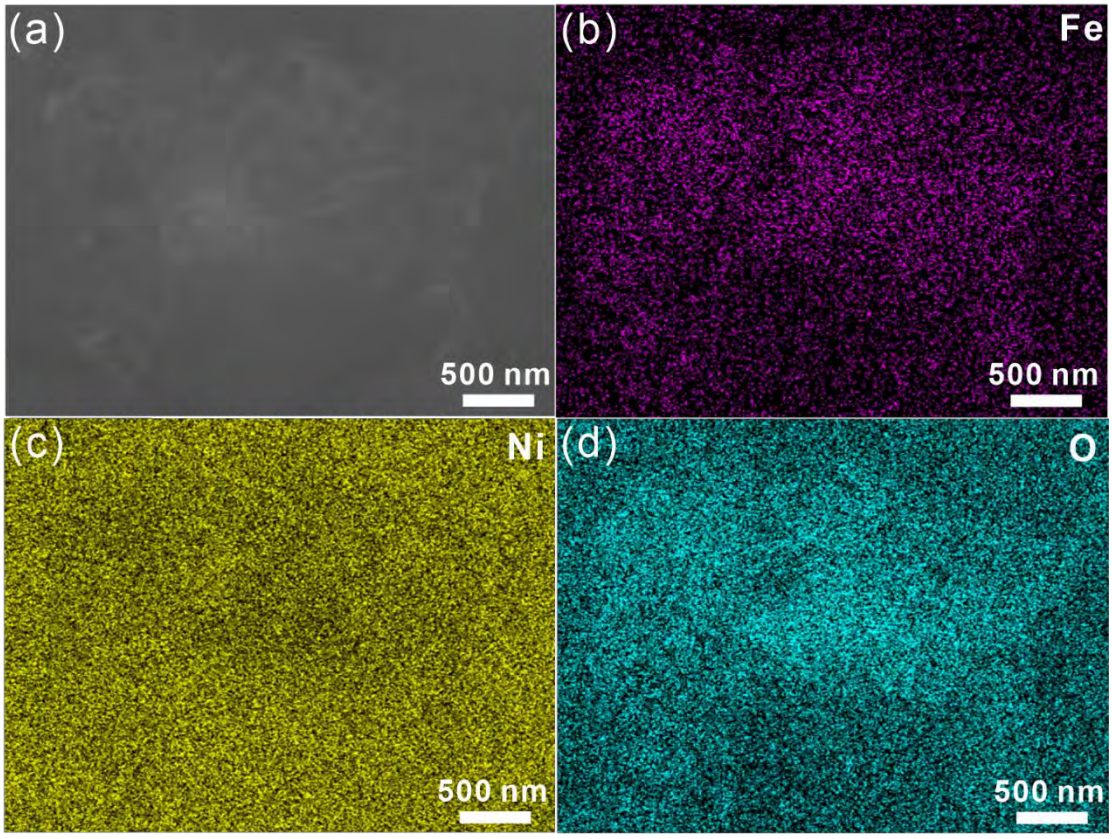

Fig. S12. EDS maps of $Ni(OH)_2$ after 50 h-CP testing obtained from the SEM equipped with the EDS detector.

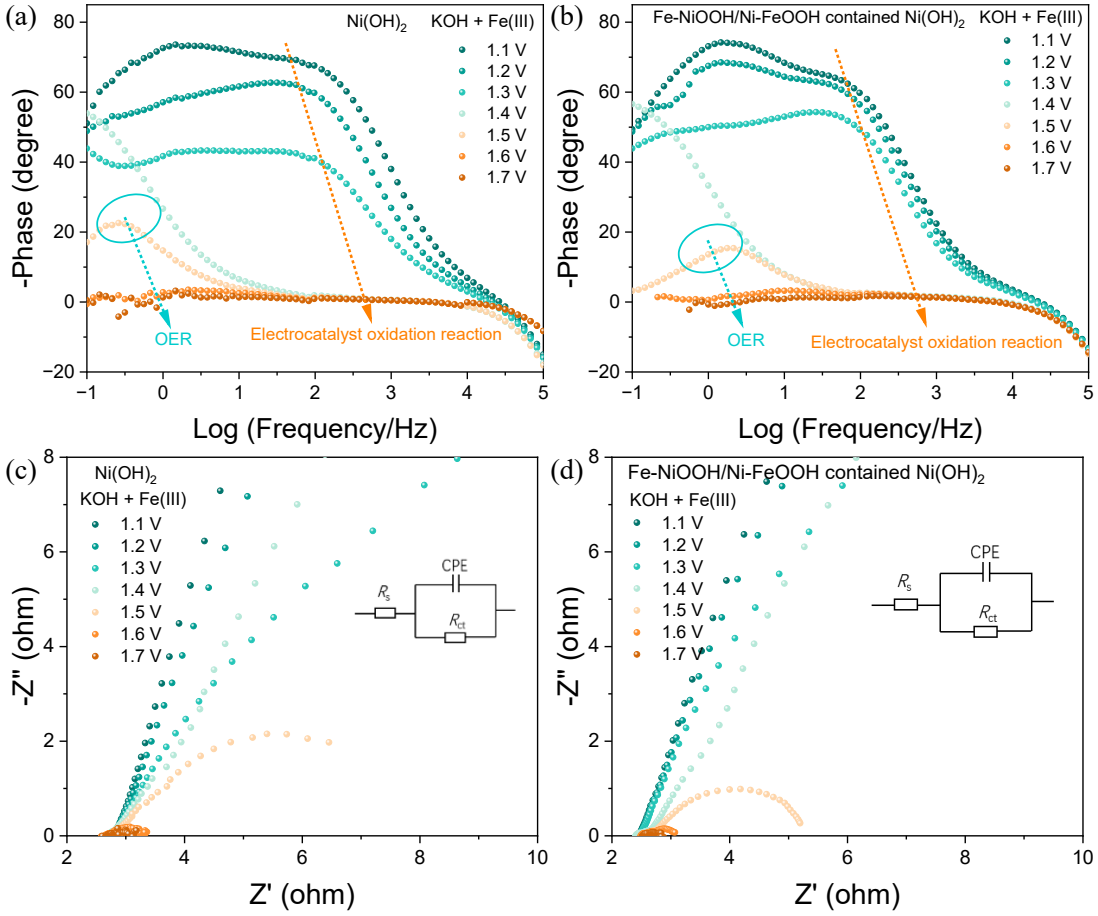

Fig. S13. (a, b) Bode-phase plots and (c, d) Nyquist plots of $Ni(OH)_2$ and $Ni(OH)_2$ with Fe-NiOOH/Ni-FeOOH construction interfaces for different applied potentials in KOH + Fe(III).

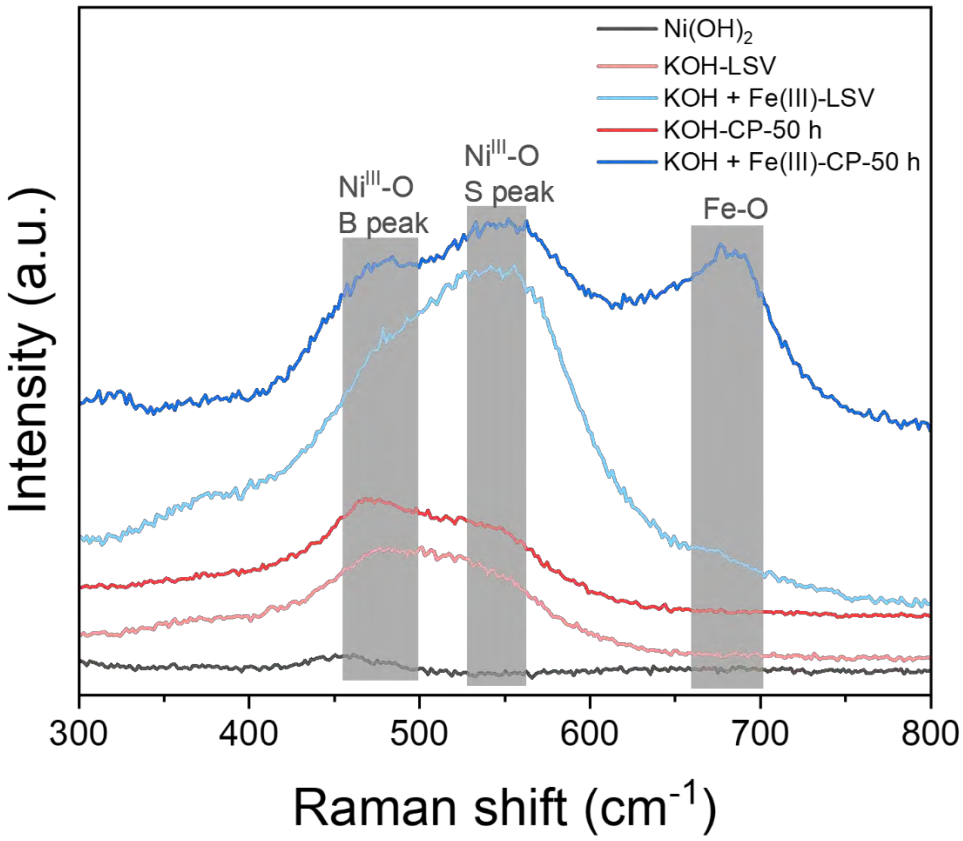

Fig. S14. Raman scattering of $Ni(OH)_2$, $Ni(OH)_2$ after the LSV test in KOH and KOH + Fe(III) as well as CP test in KOH + Fe(III) for 10 h and 50 h.

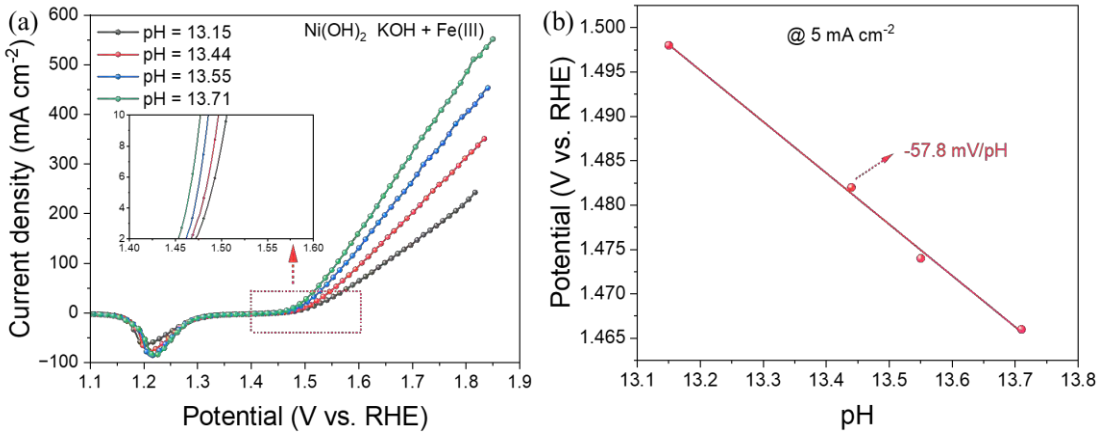

Fig. S15. (a) LSV curves (without *i*R compensation) of $Ni(OH)_2$ in KOH + Fe(III) at different pH values (13.15, 13.44, 13.55, and 13.71), (b) The potentials of $Ni(OH)_2$ in KOH + Fe(III) under different pH at current densities of 5 mA cm^{-2}. The slope corresponds to the Nernst shift.

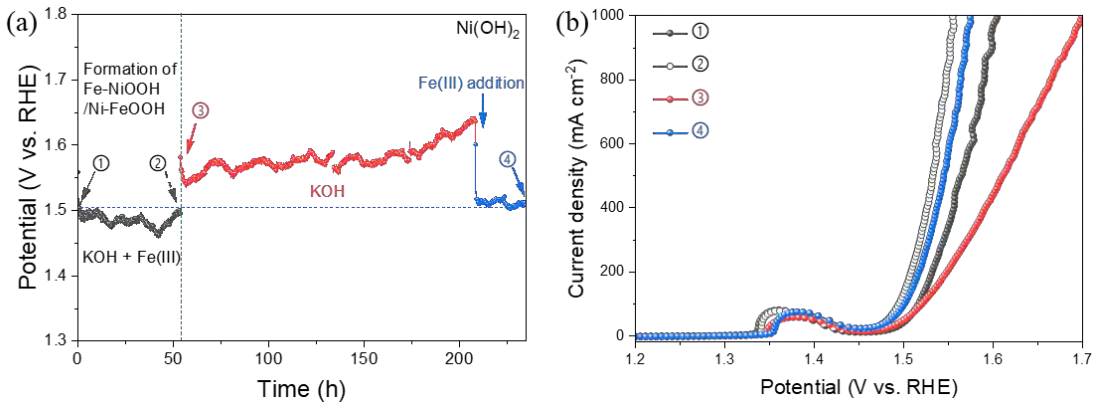

Fig. S16. (a) CP plots of the $Ni(OH)_2$ in KOH + Fe(III) for 50 h and then in KOH for 150 h, followed by another 24 h after adding Fe(III) to KOH; (b) LSV curves of the electrode obtained from the specific time indexed in the CP test (a).

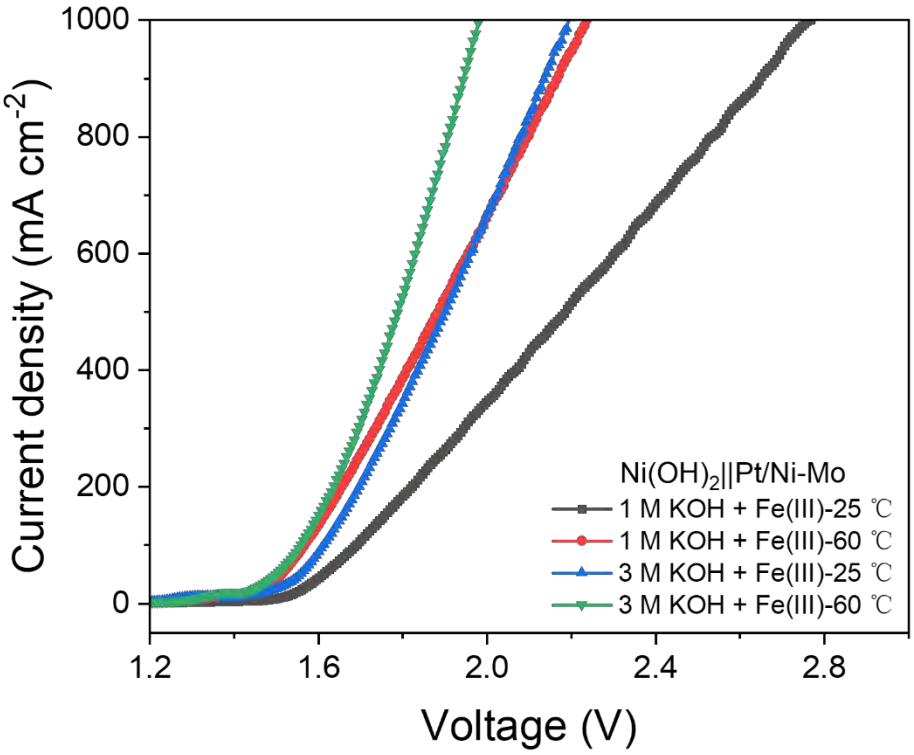

Fig. S17. The LSV curves (without *i*R compensation) of two-electrode system with $Ni(OH)_2$ as anode and Pt/Ni-Mo as cathode in 1 M, 3 M KOH at 25/60 ℃ KOH with 500 μM Fe(III).

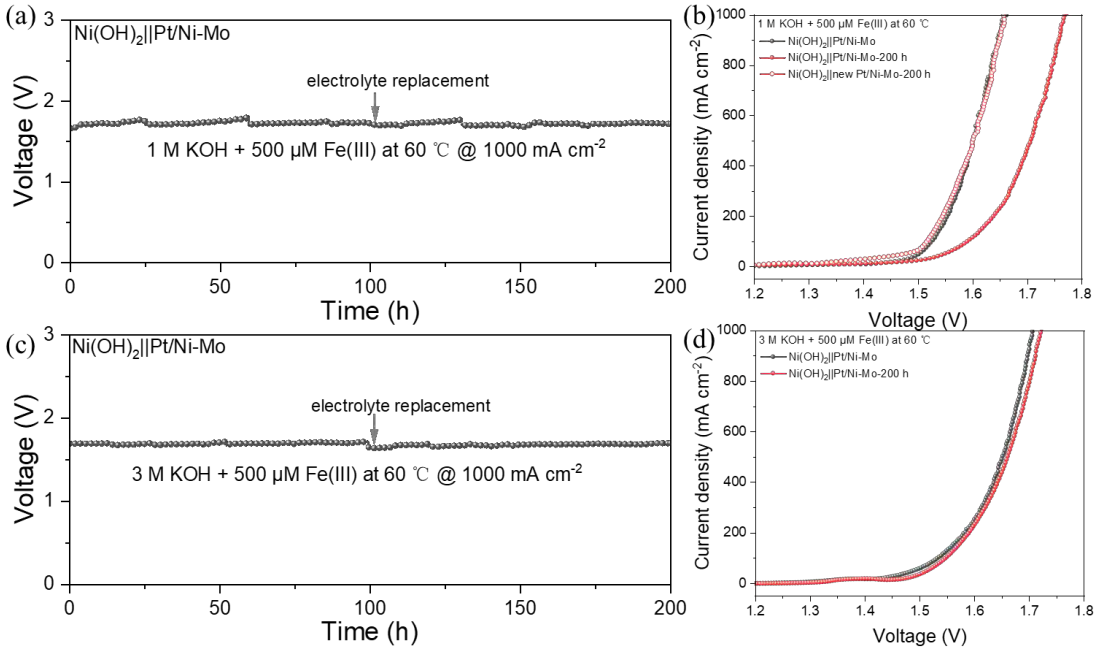

Fig. S18. The chronopotentiometry of two-electrode system with $Ni(OH)_2$ as anode and Pt/Ni-Mo as cathode in (a) 1 M and (c) 3 M KOH at 60 ℃ KOH with 500 μM Fe(III). (b) and (d) the corresponding LSV curves before and after stability test of (a) and (b).

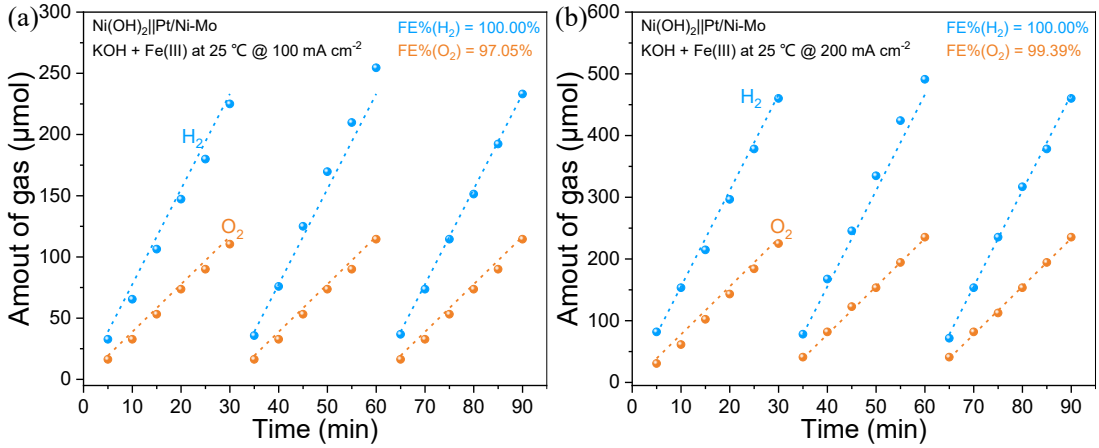

Fig. S19. Faradaic efficiency test of two-electrode system with $Ni(OH)_2$ as anode and Pt/Ni-Mo as cathode in KOH + Fe(III) at the current density of (a) 100, and (b) 200 mA cm^{-2}.